REPORT DOCUMENTATION PAGE

OMB No. 0704-0188

1. REPORT DATE (DD-MM-YYYY) 30 Sept 05	2. REPORT TYPE Final Technical Report	3. DATES COVERED (From – To) 30 Sept 05-31 Mar 08

4. TITLE AND SUBTITLE
Development of Powder Processing Models and Techniques for Meso-scale Devices: Perspirable Skin

5a. CONTRACT NUMBER

5b. GRANT NUMBER
FA9550-05-1-0202

5c. PROGRAM ELEMENT NUMBER

6. AUTHOR(S)
Patrick Kwon, Michigan State University

5d. PROJECT NUMBER

5e. TASK NUMBER

5f. WORK UNIT NUMBER

7. PERFORMING ORGANIZATION NAME(S) AND ADDRESS(ES)
Patrick Kwon
Department of Mechanical Engineering
Michigan State University
East Lansing, Michigan 48824

8. PERFORMING ORGANIZATION REPORT NUMBER

9. SPONSORING/MONITORING AGENCY NAME(S) AND ADDRESS(ES)
USAF/AFRL
AFOSR
875 North Randolph Street
Arlington VA 22203

10. SPONSOR/MONITOR'S ACRONYM(S)
AFOSR

11. SPONSORING/MONITORING
AFRL-OSR-VA-TR-2013-0913

12. DISTRIBUTION AVAILABILITY STATEMENT

Distribution Statement A: Approved for public release. Distribution is unlimited.

13. SUPPLEMENTARY NOTES

14. ABSTRACT
The Air Force will require aerospace vehicles and weapon systems with performance superior to those of any potential adversary. The establishment of a new class of thermal management materials, such as micro-textured or functionally-gradient ceramic materials, will be a key requirement for the improvement of structural performance and reliability of Air Force systems.

15. SUBJECT TERMS

16. SECURITY CLASSIFICATION OF:			17. LIMITATION OF ABSTRACT	18. NUMBER OF PAGES 11	19a. NAME OF RESPONSIBLE PERSON
a. REPORT Unclassified	b. ABSTRACT Unclassified	c. THIS PAGE Unclassified	Unclassified		19b. TELEPONE NUMBER (Include area code)

Standard Form 298 (Rev. 8-98)
Prescribed by ANSI-Std Z39-18

Final Performance Report

Development of Powder Processing Models and

Techniques for Meso-scale Devices: Perspirable Skin

Contract Number FA9550-05-1-0202

20130918434

Patrick Kwon
Department of Mechanical Engineering
Michigan State University
East Lansing, Michigan 48824
pkwon@egr.msu.edu
(517) 355-0173

EXTENTED ABSTRACT

Perspirable Skin is a new concept for Autonomous Self-cooling Multi-functional Material for Reenetry or Supersonic vehicle. The basic configuration of the perspirable skin has a peg-and-hole arrangement of two materials with distinct coefficient of thermal expansion (CTEs) that has been shrink fitted. The interference between peg and hole is designed to open when the surface temperature is high. In the application with the Reentry or Supersonic vehicle, atmospheric air bombards the surface of a vehicle causing high frictional heat flux. The interference designed to be opened at a designed high temperature, which allows compressed air to be expelled through the interference between two materials. Thus, instead of the frictional heating, the compressed air, as extracted out of the interference, is mixed with the atmospheric air, intending to eliminate most of the frictional heating. The self-regulating cooling characteristic is completely reversible as the interface will close when the surface is cooled. The design and fabrication of various materials being considered including the materials with negative CTE and a designed gradiency has been completed for the construction of Perspirable Skin. For example, the materials for the core has been designed and fabricated. For example, a composite material with a desirable CTE by combining the negative and positive CTE materials and continuous Functionally Graded Materials (FGMs) by the reaction and diffusion between two materials. We have considered two types of Perspirable skin; one with mullite core and zirconia skin and the other with zirconium tungstate (ZrW_2O_8)-based FGM core and Reinforced Carbon-Carbon Composite (RCC) skin. The former uses the difference in CTE to open the interference. For the latter, the near zero Coefficient of Thermal Expansion (CTE) of RCC in tandem with the negative CTE of ZrW_2O_8 will open the interference. Understanding of compaction and sintering behaviors of the powers were essential in the shrink-fit process for the Perspirable Skin. With the DURIP grant in conjunction with this project, a thermomechanical analyzer (TMA) and a tensile machine with dual load cells were procured. The TMA has been used extensively to construct sintering models of various powders used and to measure the CTEs of various materials in the project. The compaction experiment has been carried out using the tensile machine. The results of the compaction and sintering experiments have been presented.

1. INTRODUCTION

Biomimetics has triggered a number of technological innovations. Today, the gecko's powerful ability to cling to vertical surfaces is inspiring new types of adhesion. Exploring photosynthesis in leaves has led to the creation of transparent photocells that can absorb solar rays. The proposed perspirable skin is a bio-inspired, autonomous, self-regulating multi-functional material system for maintaining the surface temperature below a critical temperature. As human sweat to cool the body temperature, the concept used in Perspirable skin opens up the pores to cool itself. When the external surface is heated, the designed interference

between two materials arranged in peg and hole opens up due to the difference in Coefficients of Thermal Expansion (CTEs). The opened interference is used to blow compressed air onto the surface to avoid frictional heating. This concept in 2-dimensional drawing is illustrated in Figure 1.1. Two types of perspirable skin have been designed and fabricated; one with the materials with positive CTEs (e.g.: mullite core and zirconia skin) and the other with the materials with near zero and negative CTEs, (e.g.: Reinforced Carbon-Carbon Composite (RCC) and zirconium tungstate (ZrW_2O_8)–based Functionally Graded Materials (FGMs)). The former can be used when the skin is free to expand while the latter is effective when the skin is constrained as seen in the localized heating on the surface of Space Shuttle. Because of near zero CTE materials of RCC, the utilization of negative CTE materials such as ZrW_2O_8 is necessary.

(a) Core: Low CTE Material

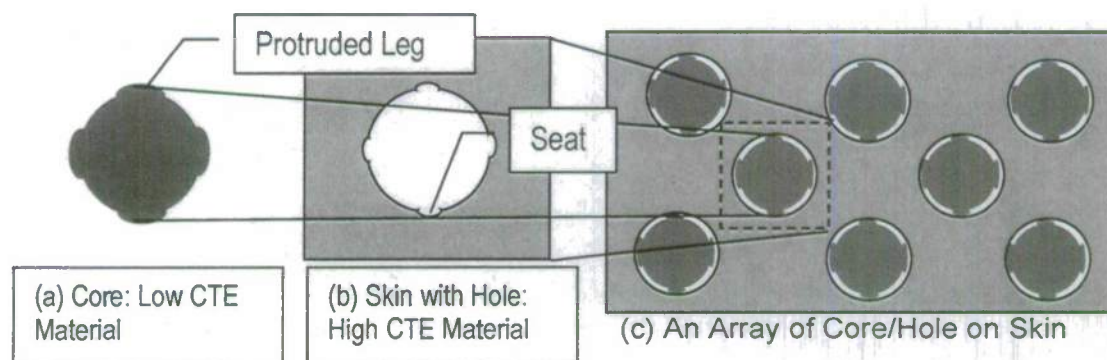(b) Skin with Hole: High CTE Material

(c) An Array of Core/Hole on Skin

Figure 1.1: The 'Core and Skin with Hole' Concept of the Proposed Perspirable Skin

When the interference of the perspirable skin is closed, the aerodynamics of flying within the atmosphere will not be interrupted. However, during the reentry into atmosphere, at the location of high surface temperature the interference will open up. This is the major advantages of the perspirable skin concept. This concept has been very successfully used in turbine blade. Small permanent holes on the surface of turbine blade are proven to be very effective to blanket the surface with cooler air as the hot combustible gas is introduced into the chamber. Here the stability of the turbine blade is not disrupted by the air flow from these holes. However, in the aerospace application, the vehicle stability may be seriously jeopardized if the aerodynamics changes due to these holes. The ideal solution is the 'skin' similar to our own. As our skin perspires to maintain our body temperature, the perspirable skin opens its 'pores' when the temperature increase substantially.

Perspirable skin can be designed to have numerous holes as shown in Fig. 1.1, which contain pegs (or cores). We expect that a gap is produced at the interface between the skin and cores when the surface reaches temperatures exceeding a designed temperature. In the application for Space Shuttle, we have to consider the use of ZrW_2O_8 as the localized heat constraints the deformation of the skin. After the background has been presented, we present the result of the compaction and sintering study of ceramic powders. The, we were able to process the step-wise FGMs, to design the perspirable skin and to process continuous FGMs.

2. BACKGROUND

For high temperature applications, we are considering many oxide ceramics and RCC composites with silica coatings to prevent oxidation. Oxide ceramics, more specifically mullite core and zirconia skin, are considered due to the higher tensile strength of zirconia. As evident in Figure 2.1 [1], the CTE of mullite is much lower that that of zirconia, alumina or magnesia allowing the interference to open up as the temperature increases. The particular perspirable skin can be useful if the boundary conditions are free (no constraint).
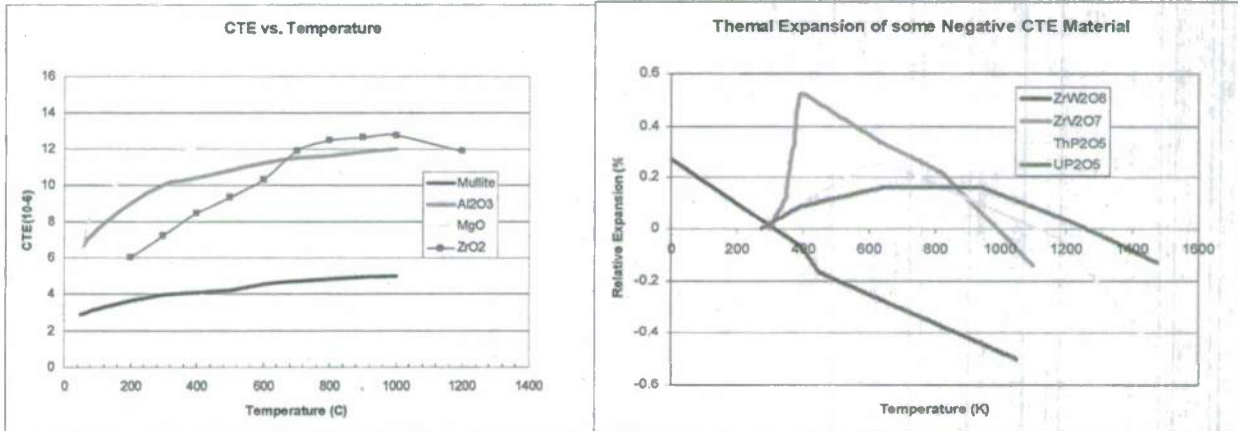

Figure 2.1: Temperature Dependency in CTE

The shrink-fit process for the skin has been developed, which makes critical to predict the dimension of the samples after partial and full sintering. As shown in Figure 2.2, the mullite core is partially sintered, machined using Computer Numerical Control (CNC) to form a shape of the skin and fully sintered. The zirconia skin is partially sintered and machined the hole for the core. The core and skin are assembled and finally sintered to achieve the core shrink-fitted into the skin. The shrink-fit process with ceramic materials demands accurate control over the dimensions on the core and skin before the shrink-fit process. Thus, the development of the compaction and sintering models is an important aspect of this research.
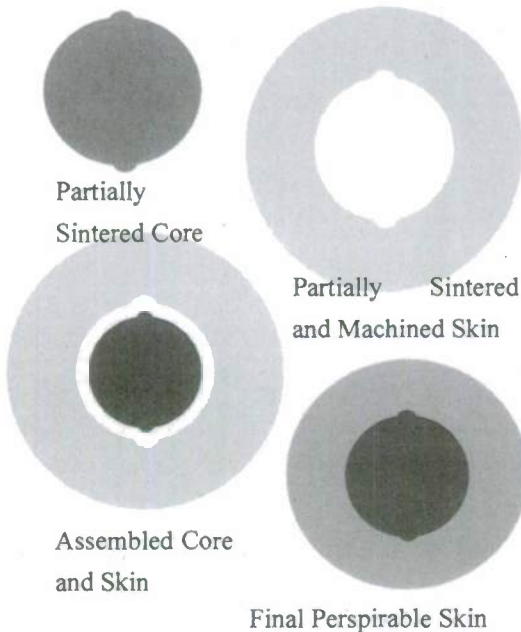
The application such as the skin for re-entry vehicle calls for a different kind of design as the heating of the skin occurs only on limited area of the skin. For such case, the core materials with negative CTEs such as zirconia tungstate

Partially Sintered Core

Partially Sintered and Machined Skin

Assembled Core and Skin

Final Perspirable Skin

Figure 2.2: Shrink-Fit Assembly of Perspiarable Skin

(ZrW$_2$O$_8$ or ZT) [2] and the skin material with near zero CTE such as RCC [3] are being considered. Figure 2.1 also contains the CTE as a function of temperature of few materials that are distinct for their negative CTEs [1-4]. The CTE of ZT is reported to be at -4.9x10^{-6}/°C [5] between 430K and 950K. In [6], the CTE of ZT reported to be as low as -13.5x10^{-6}/°C between 298 and 428K. When the negative CTE materials is used in conjunction with RCC composites which have near zero CTE, the interference between NCTE material and RCC composite can be formed. With the RCC with near zero CTE, the core will shrink to open the interference. However, because ZT melts at 1230°C, the cooling of the ZT core must be done. The CTE of the ZT measured using the TMA is similar to the reported value shown in Figure 2.1. Despite of the low level of decomposition of ZT at 780°C, the use of ZT is feasible because the quenching delays the decomposition. The level of decomposition abruptly accelerates beyond 1000°C. The XRD testing of ZT after quenching shows that no microstructural changes have occurred. The assembly of the ZT core and RCC skin is expected to be simple. The negative CTE will shrink the ZT core at a high temperature (below the decomposition temperature of 780°C). With the near zero CTE of RCC and the negative CTE of ZT, they can be assembled in a high temperature furnace.

3. COMPACTION OF CERAMIC POWDER

By mixing any two of four alumina powders, a variety of powder mixtures were produced. The relationships among relative density, stress and strain were compared for those powder mixtures in order to investigate the powder mixing effect on the compaction capability. The compaction capability was quantified by the initial relative densities. Due to the difference in the average particle size ratio between two powders as well as the compaction capability difference of the powders, the initial relative density as a function of powder proportion can be described by either a linear or parabolic curve. The essential initial powder characteristics that exhibit each curve were identified. Also, the boundaries for each initial relative density versus powder proportion curve were proposed.

3.1 Powder mixing effect on the compaction capability

In the series of experiments, four high-pure and undoped alumina (Al$_2$O$_3$) powders with submicron/micron particle sizes were investigated. The four powders were TMDAR (Taimei Chemical CO., LTD., Japan), CR-15, CR-6, and GE-1 (Baikowski Ind. Corp., U.S.A.). The detailed characteristics for the powders are summarized in Table 3.I. In the selection of the four powders, the study considered CR-15, CR-6, and GE-1, which are all from the same manufacturer, feature near identical chemical components. However, due to the difference in particle size distributions and mean particle sizes, the compaction capabilities of these three powders are quite different. TMDAR, on the other hand, was chosen because it yields a sintered product with very low porosity due to the very narrow non-lognormal range and the well-known high compaction/sintering capability. The particle size distribution for each powder was measured in a water solution by the Malvern Mastersizer Micro (Malvern Instruments, England). The results, presented in Fig. 3.1, are nearly lognormal. The micrograph from

Scanning Electron Microscopy (JEOL 6400V, Japan) clearly show that TMDAR is almost agglomerate-free while the other three powders contain agglomerates. The agglomerates of GE-1 are in flake shape while those of CR-15 and CR-6 are in near-spherical shape.

Table 3.1 Characteristics of the powders used in this study

Material	Powder	Smallest particle size (μm)	Largest particle size (μm)	Mean particle size (μm)	Mean pore size (μm)
Alumina	TMDAR	0.1	0.33	0.17	0.09
	CR-15	0.17	1.15	0.41	0.18
	CR-6	0.23	1.72	0.60	0.27
	GE-1	3.5	23.9	9.76	0.24

Material	Powder	Chemical analysis (ppm)						Bulk density (g/m^2)
		Na	K	Fe	Ca	Si	Mg	
Alumina	TMDAR	4	2	5	3	3	1	0.9
	CR-15	12	15	3	2	21	<1	0.45
	CR-6	13	22	2	3	14	<1	0.6
	GE-1	12	15	5	2	42	<1	0.45

All possible two-powder combinations were mixed in various mass ratios, and in total six powder mixture systems were produced. In addition to four unmixed powders, each system contains nine powder mixtures, in which the proportions of one powder in the mixtures range in 10% intervals. In total, fifty-four powder mixtures were studied. The powders were mixed with Speed Mixer DAC 150 (FlackTek, Inc., USA) for 3 minutes (1 minute for each cycle and totally 3 cycles) at the angular velocity of 1700 rad/s. Six grams of each powder mixture was measured by Adventurer AR 2140 (Ohaus Corp. USA) with a 0.0001g resolution; and

Figure 3.2: Particle Size Distribution of the Powders Used

then poured into a single-action die made of 1144 Stress Proof steel. The inner diameter of the die, D_{in}, is 22.19mm. Before pouring the powders into the die, the die wall was lubricated with graphite powder (Panef Corp., USA).

The top surface of the powder was flattened and then the top punch was inserted into the die until it touched the powder. The compaction load was applied on the top punch by MTS Insight 300 (MTS Systems Corp., USA). The speed was 10mm/min and the stress resolution
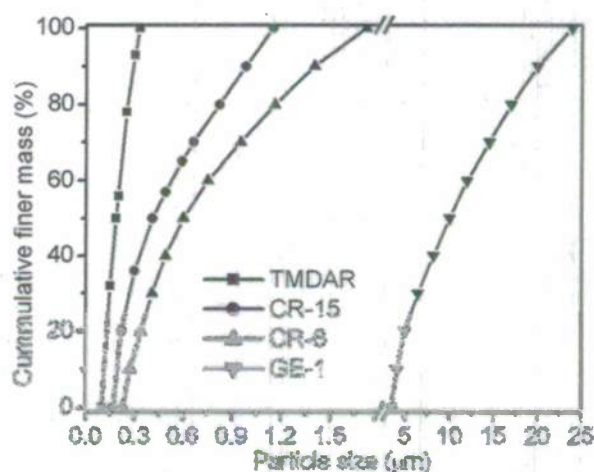
is 0.013MPa. During the compaction, only the top punch moved. The compressive forces applied on the top (F_t) and bottom punches (F_b) as well as the displacement of the top punch (Z_t) were recorded continuously as a function of time by the load sensors. The preload of 0.5MPa is necessary to measure the compact characteristics accurately before starting the main compacting process. After pre-loading, the initial height of each sample, h_i, was measured. This was done by measuring the total height of the two punches and the pre-loaded compact inside the die, then subtracting the height of the two punches. The measurement was achieved by Marathon electronic digital caliper with a 0.02mm resolution and a 150mm measurement range. Considering the diameter of each compact to be the same as the inner diameter of the die, D_{in}, the initial relative density, R_i, can be calculated by the following equation:

$$R_i = \frac{\rho_i}{\rho_f} = \frac{m/V_i}{\rho_f} = \frac{m}{\dfrac{3.975}{4}\pi D_{in}{}^2 h_i} \qquad (3.1)$$

where m, V, and ρ represent mass, volume, and density, respectively, and the subscripts i and f represent initial and theoretically fully value. The theoretical fully-density of alumina was taken as 3.975g/cm^3.

After obtaining the initial relative density, the die set with pre-loaded compact was put back into the load frame, and then the load of 80MPa was applied to compact samples. The final green samples produced a diameter of 22.19mm and their heights ranged from 7.05mm to 9.1mm. Thus, the height/diameter ratios of compacts were between 0.3 and 0.4. By keeping a low height/diameter ratio, the transmit force applied on the bottom punch and the applied force on the top punch were almost identical in the compaction. The discrepancy between the two recorded forces was less than 0.2%. The masses of the green samples were measured again after compaction. There was always an expected mass change due to the attachment of powders to the die wall and the punches as well as the powder loss during the transport. However, this change was very small, less than 0.4%, and was neglected. Several green samples were coated with nail polish and then their volumes were measured in water by Archimedes' principle. Those values were then compared to the corresponding volumes calculated by the final sample heights, h_f, and diameter, D_{in}. The discrepancies between the two groups of values were minimial, less than 1.1%. Therefore, only the calculated volumes are reported in this investigation.

By the recorded top punch displacement, Z_t, and the initial compact height, h_i, or final compact height, h_f, the sample height, h_t, at time t can be calculate. From the calculated h_t, similar to calculating the initial relative density, the relative density at time t, defined as R_t, can be found as,

$$R_t = \frac{\rho_t}{\rho_f} = \frac{m/V_t}{\rho_f} = \frac{m}{\dfrac{3.975}{4}\pi D_{in}{}^2 h_t} \qquad (3.2)$$

In Eq. (3.2), the sample diameter was assumed to match the inner diameter of the die, D_{in}. The corresponding stress, σ_t, at time t can be obtained by the punch diameter, D_{in}, and the

recorded load, F_t.

$$\sigma_t = \frac{F_t}{S_t} = \frac{F_t}{\frac{1}{4}\pi D_{in}^2}$$

(3.3)

where S_t is the cross-sectional area of the top punch.

The relative density-stress curves for each mixture group were drawn. Figure 3.3 a & b show the representative curves for the TMDAR+CR-15 and CR-6+GE-1 powder mixture groups, respectively. For clarity, only six curves were included.
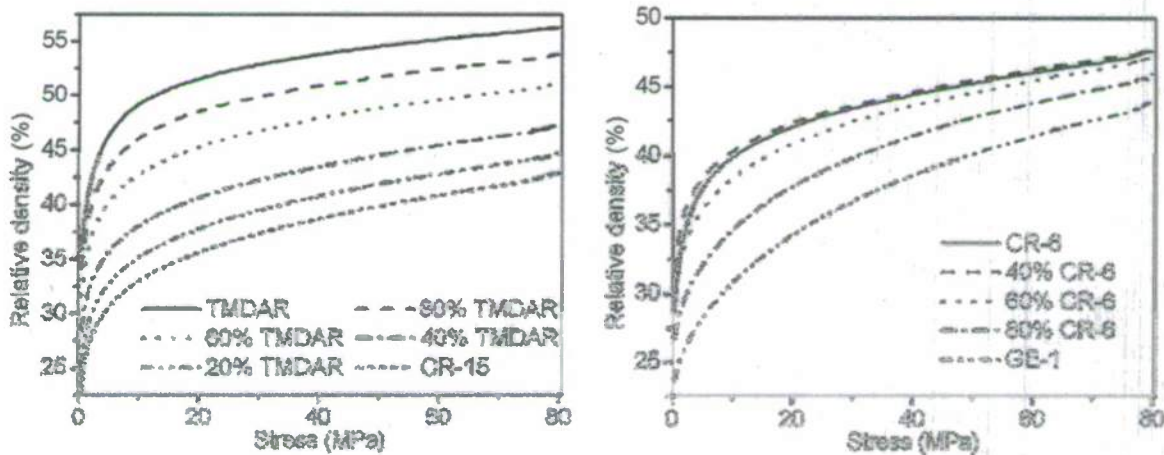

Figure 3.3: The relative density-stress curves for a) CR-15+TMDAR and b) CR-6+GE-1

A higher relative density represents improved compaction capability. Even the absolute relative density values continuously increase with the increase in the compaction load, the relationship between the relative density and powder proportions remains similar for each powder mixture group as observed in Figure 3.3. Therefore, one can conclude that the starting powder combination determines the compaction capability of each powder mixture. In addition, the initial relative densities dictated by the starting powder combination can be used to quantify and compare the compaction capability of each powder mixture.

The relationships between the initial relative density and the powder proportion are shown in Figure 3.4 for all six groups. For each curve, the left end is the 100% of the fine powder and the right end is the 100% of the coarse powder. Figure 3.4
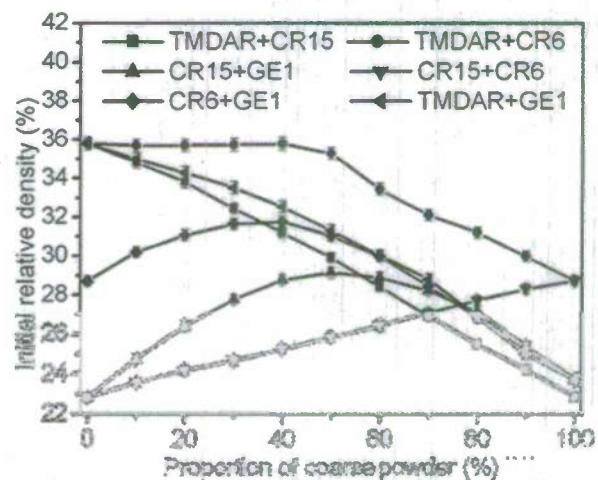

Figure 3.4: The initial relative density –powder proportion for all six groups with 0.5MPa pre-load compaction.

shows two kinds of relationships between the initial relative density and the proportion of the coarse powder.

1) Linear relationship: TMDAR+CR-15 and CR-15+CR-6 powder mixture groups show this characteristic. The maximum relative density corresponds to 100% of one of the powders.

2) Nearly parabolic relationship: The maximum relative density of some powder groups with this relationship occurs with certain powder mixtures, such as TMDAR+CR-6, CR-15+GE-1, and CR-6+GE-1. This is similar to the conclusion of Westman and Hugill [7] and McGeary [8]. However, the proportions of coarse powder in the powder mixture that attained the maximum relative density are between 40% and 60%. These values differ from the reported 30% by Westman and Hugill [7] and McGeary [8] for sand and metal balls. Another powder system, TMDAR+GE-1, has the maximum relative density at 100% TMDAR.

3.2 Relative density-strain relationship for various powder mixtures

Aydin *et al.* [9, 10] defined axial true strain $\bar{\varepsilon}_t$ as the following,

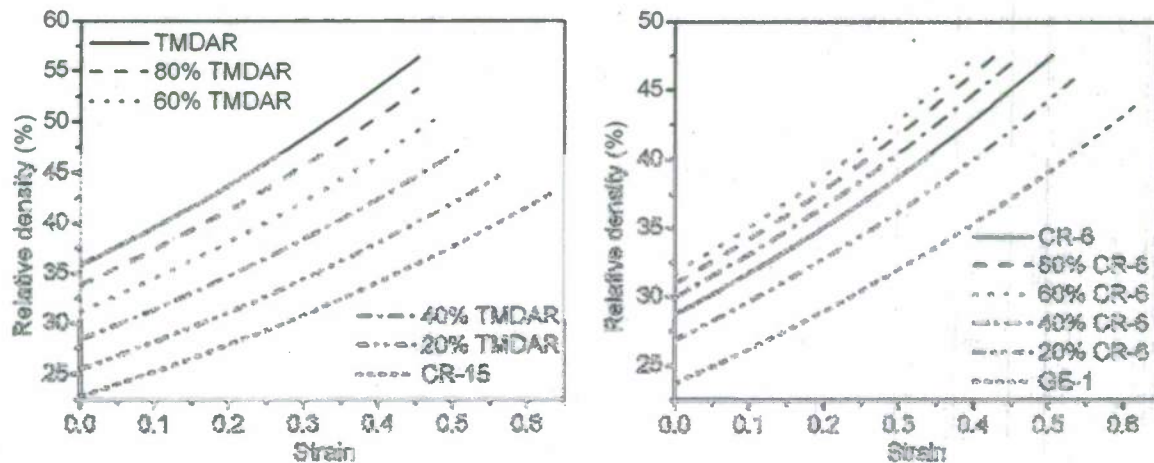$$\bar{\varepsilon}_t = \left| \ln(\frac{h_t}{h_i}) \right| \tag{3.4}$$

Figure 3.5: The relative density-strain curves for a) CR-15+TMDAR and b) CR-6+GE-1.

Figure 3.5 show the representative relative density-strain curves for the TMDAR+CR-15 and CR-6+GE-1 powder mixture groups, respectively. The powder mixture with a better compaction capability/density in Figure 3.4 is also with a higher relative density under any strain values in Figure 3.5. The relationship exactly fits into the following equation for each powder mixture,

$$R_t = \kappa e^{\bar{\varepsilon}_t} \tag{3.5}$$

where κ has the same unit as density, g/cm³. Eq. (3.5) shows that a powder mixture with a higher density/compaction capability has a larger κ value. Table 3.2 displays the κ value for the TMDAR+CR-15 powder mixture group. The values in Table 3.2 are the same as the

corresponding initial relative density value in Figure 3.5. This indicates the physical meaning of κ in Eq. (3.5) is the "initial relative density". Thus, the conclusion can be made as

$$R_t = R_i e^{\overline{\varepsilon}_t} \tag{3.6}$$

Therefore, one can use Figure 3.5 to find the difference in the compaction capabilities of powder mixtures. It is important to emphasize that the initial relative density is dependent on the pre-load. For example, when the pre-load reduced to 0.3MPa, the initial relative density for pure TMDAR was changed to 30.46%. If the stress/strain goes to zero, the initial density goes to the bulk density listed in Table I. However, even the absolute value of the initial density varies, the relationship between the relative density and strain remains equivalent to Eq. (3.5) and the order of compaction capability/relative density remains unchanged.

Table 3.2. The coefficient k in Equation (7) for each TMDAR+CR-15 powder mixture

CR-15	0%	10%	20%	30%	40%	50%	60%	70%	80%	90%	100%
$\kappa\,(g/cm^3)$	1.4228	1.3843	1.344	1.29	1.2401	1.1887	1.1296	1.0688	1.0131	0.9622	0.908

3.3 Prediction of initial relative density versus coarse powder proportion curve shape from the characteristics of powders

Since the four powders used are the same material with nearly identical elements, the linear and parabolic types of curves in Figure 3.4 may be a result from the difference in the particle size distributions and mean particle sizes. Numerous studies [7, 8, 11] mentioned that if fine particles can fill into the interstices among coarse particles, then the powder mixture should produce a better compaction capability. In this condition, the total volume does not necessary change with the addition of fine powder(s). This will be stated as a "non-disturbance" condition. For a bimodal discrete sphere size system, the particle size of coarse powder is at least 2.4 times of that of fine powder [9] to make a "non-disturbance" powder mixture. More strictly, the condition, $\overline{D}_c / \overline{D}_f > 6.5$, is required for the non-disturbance mixing [9, 11], where $\overline{D}$ represents the average particle size and the subscript, c or f, represent coarse or fine powder, respectively. For a continuous size distribution system, the limitation average particle size ratio value is approximately 3.6 [12, 13].

If the average particle size ratio is less than 3.6, the fine powder cannot fill within the interstices of the coarse powders. The
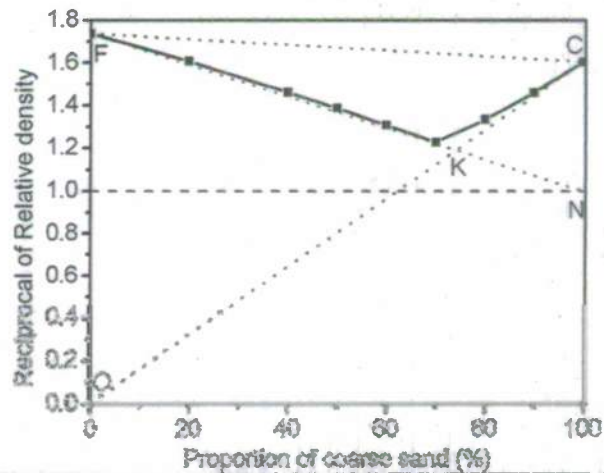

Figure 3.6: The dependence of the reciprocal of relative density on the proportion of coarse powder and its triangle boundary by Westman et al. [4].

mixing of the two powders only results in stacking them together mechanically. Therefore, the relative density-powder proportion curve would be linear. Among the powder mixture systems we employed, TMDAR+CR-15 and CR-15+CR-6 show this trend. The corresponding linear curves in Figure 3.4 verify this assumption. However, the agglomerates in some powders may influence the pore/particle size and result in partial filling of fine particles into coarse particles. The agglomerates may be the reason why some parts in those two curves are not perfectly linear.

If the average particle size ratio is larger than 3.6, the mixtures always will not have better compaction capability than each powder based on Table 3.1 and Figure 3.4. For example, the $\overline{D}_c / \overline{D}_f$ of TMDAR+GE-1 powder mixture group equals 57.4. However, its highest density happens with pure TMDAR. This is due to the large difference in the compaction capabilities of the two powders. The initial relative density difference between TMDAR and GE-1 is as large as 12.1%. This shows that even the TMDAR does fill into the interstices of GE-1; the increase in the compaction capability due to the interstitial filling is negligible compared to the excellent compaction capability of TMDAR. Therefore, the excellent compaction capability of TMDAR dominates the compaction of the mixture, resulting in the highest density with pure TMDAR.

For the remaining three mixture groups with parabolic curves shown in Figure 3.4, the difference in the initial relative density between two powders ranges between 0.87 and 5.9%. In the three curves, the difference in the relative densities are small enough to be compensated by filling fine powder into the coarse powder, thus producing mixture(s) that have better compaction capability than the two powders. The Maximum Compaction Capability (MCC) occurs at 40-60% proportion of coarse powder, close to the powder with better compaction capability. When the difference in compaction capability between the powders increases, the

Figure 3.7. The dependence of the initial density on the vibration time

proportion of powders at MCC shifts closer to the powder with better compaction capability. As seen in other powder mixtures, once the compaction capability difference between the powders exceeds a threshold, the peak converts to the powder side with better compaction capability (for example, TMDAR+GE-1). From the TMDAR+CR-6, CR-15+GE-1, CR-6+GE-1, and TMDAR+GE-1 powder mixture groups, the threshold may be in the 8-10% relative density range.

The discussion above allows us to conclude that the straight line passing through both powders' initial relative densities sets the lower boundary for an initial relative density - powder proportion curve. Can the upper boundary also be found? In Westman and Hugill's
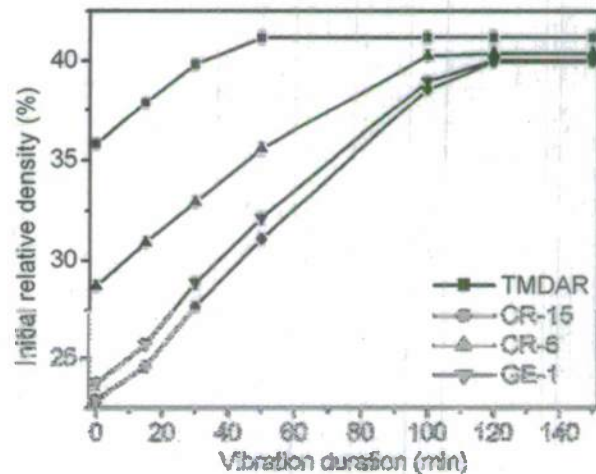
study [7], the reciprocal of relative density of the compact was used to quantify the compaction capability of various sand mixtures. By assuming the fine powder is infinitesimal, one lower boundary was proposed for the curve, as the CO line in Figure 3.6. By assuming a larger ball immersed in the infinitesimal balls/water, the other lower boundary FN was obtained. The study concluded that the reciprocal of relative density - powder proportion curve should lie in the triangle CFK.

Based on Westman and Hugill's idea, the O and N points in Figure 3.6 should convert to the maximum initial relative density of the powders in the initial density versus powder proportion curves. To obtain these maximum initial density values, each powder was put into the die set and then the die set was put on a plane sieves vibrator (Thomas Scientific, USA). The frequency of the vibration was set to 60Hz and the amplitude was set to 4mm. During the vibration, the particles rearranged to an optimal arrangement. The die set was then moved to the MTS machine and the powders were compacted to the 0.5MPa pre-load. Figure 3.7 shows the dependence of the initial relative densities of the four powders in relation to the vibration time.
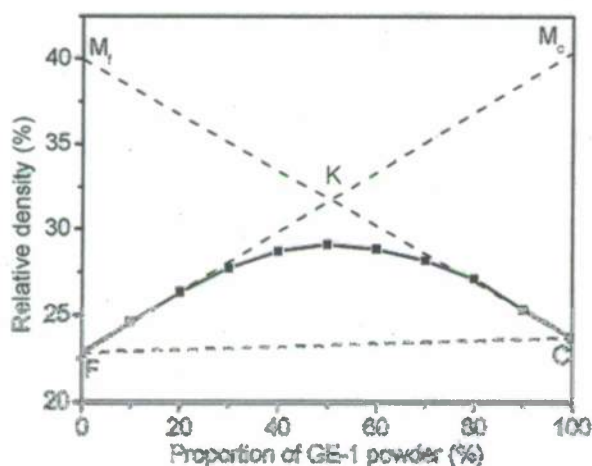

Figure 3.8: Triangle boundary for the initial relative density-powder proportion curve of CR-15+GE-1 powder group.

Clearly, as a result of the particle rearrangement caused by the vibration, the initial relative density increases for each powder. The density increases with vibration duration, and converges to a final value. Each final value is considered to be the maximum initial relative density value for the corresponding powder.

The lines, FM_C and CM_f, in Figure 3.8, are obtained by connecting the relative density of the fine powder to the maximum relative density of the coarse powder and the relative density of the coarse powder to the maximum relative density of the fine powder, respectively. These two lines will build the upper boundaries for the initial relative density-coarse powder proportion curve of CR-15+GE-1 powder mixture group. And the triangle FCK creates the enclosed boundary. Figure 3.9 shows the triangle boundaries for TMDAR+CR-6 and CR-6+GE-1 powder mixture groups. Clearly,
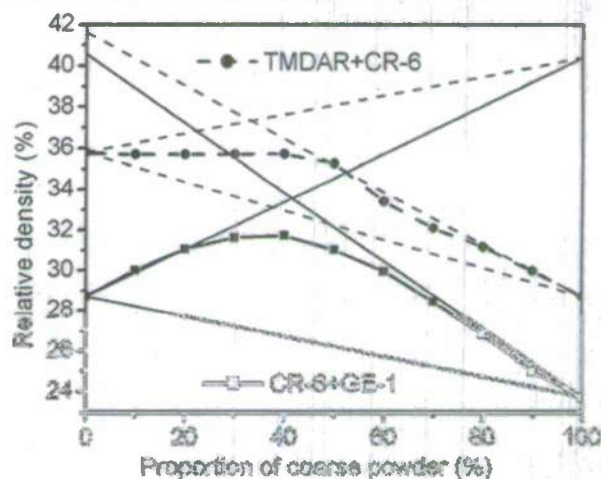

Figure 3.9: Triangle boundaries for the initial relative density-coarse powder proportion curves of TMDAR+CR-6,

as CR-15+GE-1, each initial relative density versus coarse powder proportion curve in Figure 3.9 also lies within the corresponding triangle.

3.4 Discussion about the maximum packing/compaction relative density

Brouwers [14] proposed an analytical expression to calculate the void fraction/packing density of continuous particle distribution powders of the lognormal type, which is

$$\varphi = \varphi_1 (\frac{d_{max}}{d_{min}})^{-(1-\varphi_1)\beta/(1+\alpha^2)} \tag{3.7}$$

where ϕ is the void fraction of the powder with continuous particle size distribution, d_{max} and d_{min} represent the maximum and minimum particle sizes, respectively. ϕ_1 is the void fraction of assumed uniformly sized particles with the average particle size, α is the distribution modulus, and β is the scaled gradient of the void fraction. Commonly, both ϕ_1 and β can be set as constant, and in Brouwers' study ϕ_1 =0.5 and β = 0.35 for fairly angular quartz. The distribution modulus α is typically between 0 and 0.37. When α equals 0, the maximum packing fraction is obtained. Using the Brouwers' parameter setting of ϕ_1 and β, the range of maximum relative packing densities of each powder was calculated and presented in Table 3.3.

To attain the maximum compaction density from the experiments, 3g of each powder was vibrated for 150min and then compacted to 220MPa. After 180MPa compaction, the relative densities were convergent to maximum values. Those experimental maximum relative densities are also listed in Table 3.3. For CR-15, CR-6, and GE-1 powder, the experimental values are less than the calculated values. Two reasons contribute to the lower experimental results, 1) the ϕ_1 and β may not be exact for our powders, and 2) the agglomerates presented in the powders and the non-perfect spherical-shaped powder particles [15]. However, the order of the relative density/compaction capability among these three powders is the same in both the calculation of Brouwers' equation and the experiments. From this point, the Brouwers' equation has an excellent potential for predicting the compaction capability of various powders.

Table 3.3. The maximum relative packing density (Brouwers' equation vs. experiments)

		TMDAR	CR-15	CR-6	GE-1
Calculated results	α=0	59.4%	64.2%	64.9%	64.3%
	α=0.37	58.4%	62.7%	63.3%	62.8
Experimental results	150min vibration	59.8%	52.5%	53.3%	52.7%

Contrary to CR-15, CR-6, and GE-1 powders, the experimental result for TMDAR is larger than the calculated result. As mentioned before, Brouwers' equation is suitable for the powder systems with lognormal particle distribution. However, the particle size distribution of TMDAR is not lognormal. Thus, the Brouwers' equation is not suitable to calculate its compaction capability. The non-lognormal size distribution powder systems have increased maximum

packing fractions than lognormal distributed powders [15]. Thus, the compaction capability of TMDAR is improved compared to the other three powders. Therefore, when using Brouwers' equation to evaluate the compaction capability of powders, the particle size distribution of each powder should be lognormal.

3.5 Dimensional variation by compaction

Due to the series of operation steps, the green samples contain a degree of structural inhomogeneity, namely, density variation and the dimensional variability [9, 10, 15-19]. The latter is the geometry of the external surface of the ceramic green body which is invariably not exactly the same or a simple linear scale transformation of the shape of the terminal geometry of die cavity after the green ejection. Important questions remain regarding the evolution of the external shape of the green compacts during the compaction process.

The external shapes of several green samples achieved in Section 3.1 were measured. The measurements were preformed by Veelo-DEKTAK 6M Stylus Profiler at Fraunhofer CCL. The resolution is 0.5nm. A specially designed base was used to support samples as shown Figure 3.10. The diameter in the base is same to the inner diameter of the die. After a sample "sat" on the base, the probe of the profiler touched the external surface of the sample. A 3mg force was applied on the probe and then the probe moved from one edge to the other edge to measure the external surface profile. After one measurement, the sample was rotated 90° on the base and another measurement was performed. Totally four measurements were achieved on each sample.

By taking average value of four measurements, the diameter variation along the thickness direction was obtained for each sample. Figure 3.11 shows the diameter variation of GE-1 sample.

All samples feature the similar barrel lateral shape. By finite element analysis, Aydin et al. [10] found after compaction, the green samples inside the die have large residual radial stress around the middle of
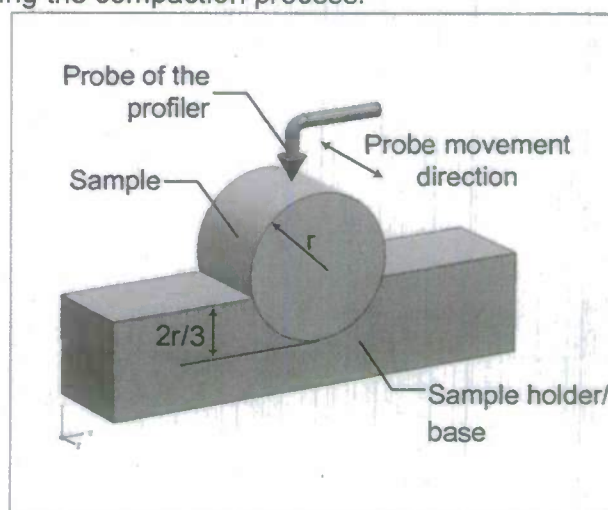

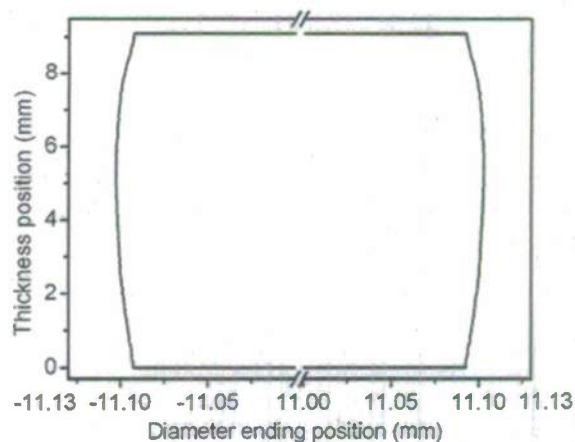Figure 3.10 The schematics of external shape measurement

Figure 3.11 The diameter variation along the thickness direction of GE-1 samples

the compact, and small redial residual stress on the top and bottom surface. After the ejection of the green sample, the compact is free in the radial direction. Therefore, the high stress regions relax radically, resulting larger diameter regions in the final greens. And finally the lateral shape of green sample are similar to a barrel.

For GE-1 sample, the difference between the largest diameter and smallest one is 20.631um. This difference varies with different samples. Figure 3.12 shows the diameter difference varies by the different powder component for the CR15+GE1 and TMDAR+CR15 groups.

Comparing Figure 3.12 to the corresponding powder groups in Figure 3.4, it is easy to see that powder mixtures with a better compaction capability yielded a smaller diameter difference. Powder with a better compaction capability results shorter green samples if the powder masses are same. Therefore, the residue stress distribution difference insider the green samples hold by the die will be smaller for a

Figure 3.12 Dependence of largest and smallest diameter difference on the powder proportion.

powder compact with a better compaction capability, resulting a smaller diameter difference.

More interesting, the curves in Figure 3.12 have a near "mirror image" relationship to the responding curves in Figure 3.4. This relationship is very important, since we can estimate the dimension variation of green samples made by powder mixtures based on the compaction capability relationship in Figure 3.4 and the tested diameter difference of the two ending powders.
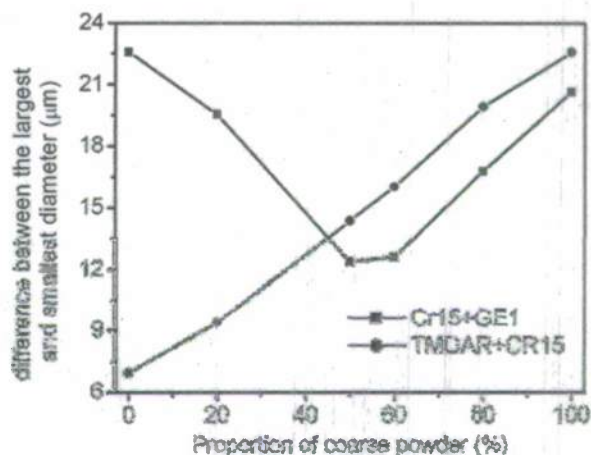
3.6 Density distribution by compaction

As mentioned in Section 3.5, the densities of a green sample are not even everywhere, but with a density distribution. Aydin et al [9, 15] designed an experiment, in which they used lead balls as tracers to detect the densification. However, this method only put the tracers in several positions, not in a continuous way. To overcome this disadvantage, we used colored powder as tracer to investigate the density distribution insider green compacts.

In Section 3.1, we already discovered that powder mixing can change the compaction capability. Therefore, we dyed several powder mixtures by stamp-ink (2000 plus, Red, COSCO, Germany). The mixtures then were put into a furnace (Carbolite-HTF1700, UK) for 4 hours at 70°C to dry out. The remaining solids were put into bottles with 12mm diameter alumina mixing media. The bottles were on a jar mill (U.S. Stoneware 764AVM, U.S.A.) for 48 hours to break the solids. Then the powders were sifted to sort colored powder with size less than 0.3mm. The colored powders were compacted to 0.5MPa to get the initial densities in the

way mentioned in Section 3.1. Then the values were compared with pure TMDAR, 50/50 TMDAR/CR15, pure CR15, 50/50 CR15/GE1 and pure GE1. The colored powder with same compaction capability to a powder mixture will be used as its compaction indicator.

To investigate the density distribution insider a green compact, the height of the green sample cannot be two small. In this study, we keep the height/diameter ratio of each green sample around 1.1-1.2. The diameter of the samples is around 22mm. In the experiments, we kept the thickness of each main powder layer and each colored powder layer identical. And the thickness of the colored powder layer is around 1/15 of the main powder layer. Based on these requirements, the powder mass of each layer can be calculated. The main powder is 1.2-2g of each layer depending on different powders. And the colored powder mass is between 0.1-0.2g each layer.

Similar to the compaction procedure in Section 3.1, the first layer powder, which always is main powder, was pour into the die, which was lubricated with graphite powder (Panef Corp., USA) into the die until it touched the powder. After a pre-load of 0.5MPa, the die set was moved from the MTS (MTS Insight 300, MTS Systems Corp., USA). The layer thickness, measured by subtracting the height of the two punches from the total height of the two punches and the pre-loaded compact inside the die, was recorded. The top punch was then dragged out of the die slowly. The second layer powder (colored powder) was pour into the die. After painting the surface of the layer, the top punch was put back into
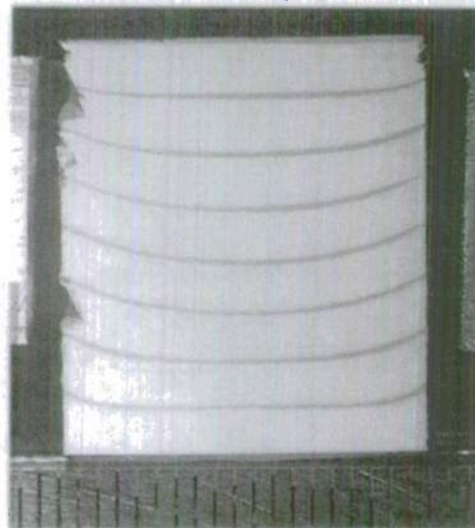

Figure 3.13 the photo of the middle section of a TMDAR sample. The bottom side in the picture is the side contacting the bottom punch in the compaction.

the die. The 0.5 MPa pre-load was applied on the both layer again. Repeat the procedure till the last layer was pre-loaded. And then the load of 80MPa was applied to compact samples.

The green samples were then took out the die and polished carefully on the lateral surface till to the middle section. Then each sample sat on the sample base mentioned in Section 3.5. The photos were taken by a microscope (Wild M5A, Wild Heerbrugg Ltd, Switzerland). Figure
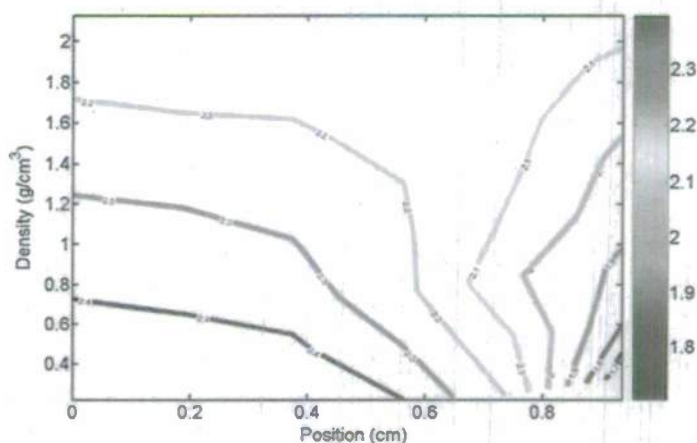

Figure 3.14 The density distribution of TMDAR green sample, 0 position is the radial symmetric axel in Figure 3.13.

3.13 shows the picture of TMDAR.

In Section 3.2, the relative density p_t can be calculated by:

$$\rho_t = \rho_i e^{\left| \ln\left(\frac{h_t}{h_i}\right) \right|}$$

where p_i is the initial density after 0.5MPa. h_i is the initial height of each layer, which is recorded after each pre-compaction and h_t is the final height of a position, which is obtained by analyzing the photo by software IMAGE G. Since the each indicator layer is curved after compaction as shown in Figure 3.13, the h_t is varied by positions.

The density distribution contour was calculated and plotted by MatLab, Figure 3.14 shows the contour of TMDAR, in which the 0 position is corresponding to the center axial in the Figure 3.13. Clearly the high-density regions exist at the near the bottom central region and on the central axis. And the low-density regions are at the bottom edges and near the top center. Our results are similar to Aydin et al [9,15] and others' report [16-19]. All other powder compacts feature similar density distribution contour as shown in Figure 3.14. However, the density distribution range varies as different powders. For powders with better compaction capability, both lowest density and highest density are larger than corresponding values of the compact with lower compaction capability.

4. SINTERING OF CERAMIC POWDER

The sintering models being developed can be classified as phenomenological approach first developed by [21-24]. This work is unique because the sintering models influenced by various powder characteristics have been studied. For the alumina work, two distinct alumina powders, TMDAR (manufactured by Taimei Chemical CO., LTD.) and CR-15 (manufactured by Baikowski Ind. Corp.), are used, whose powder characteristics are shown in Table 4.1. Beside the average powder size of CR-15 is much larger that of TMDAR. The typical application of CR-15 is in polishing. CR-15 also has much higher sodium, potassium, and silicon concentration which results the uneven grain size distribution in system with CR-15 [25, 26]. In addition CR-15 contains 10% γ–alumina phase. These differences make these two powers ideal for the development of sintering model.

Table 4.1: Powder Characteristics of Alumina Powders

Powder	Mean particle size (μ m)	Alpha content (%)	Chemical Analysis (ppm)					
			Na	K	Fe	Ca	Si	Mg
TMDAR	0.17	100	4	2	5	3	3	1
CR-15	0.42	90	13	22	2	3	13	1

Figure 4.1 shows the particle size distribution analysis results of various powders used. TMDAR powder has only one distinct peak, much narrower particle size distribution and finer particle size while the as-received CR-15 powder has two peaks in the particle size distribution, much wider particle size distribution and coarser particle size. Even though not shown here, the SEM images verify agglomerates in CR-15. With at least 24 hrs of ball-milling, the peak with larger particle size drop for CR-15 which means that the milling breaks some agglomerates. Additional peak in the powder distribution was evident in the third plot in Figure 4.1. This is believed to be the results of the

Figure 4.1. Particle size distribution profile of powders used in this study.

"loose packing" of the small particles. The proportion of agglomerations in the ball-milled CR-15 is less than that in the as-received CR-15. Distinctively, the TMDAR is almost agglomeration-free. Sintering behavior has been studied with the TMA machine. This machine has the rod in contact with the sample to measure the change in dimension under various temperature cycles. The total testing range of this TMA machine is ±2000um, and even considering the reaction between rod and sample, the error for displacement test is claimed to be less 4% [22]. During our experiments, 5g force is applied to insure the contact between rod and sample.

Figure 4.3 shows the relationship between densification rate and relative density for the combination of TMDAR and CR-15 alumina powder system. All the experiments were executed in the same condition: the compacting pressure of 200MPa, the sinter temperature of 1500°C, Argon gas in the sintering environment and the temperature ramp rate of 6°C/min. The green bodies have the same dimension: 7.94mm in diameter and 7.94mm in height. Each curve has the ascending and descending parts. Except pure CR-15 sample; all other samples are almost full-sintered (the relative density (RD) greater than 95%). Even though the SEM pictures are not presented here, they easily visualize the trend of this final density change with the change in TMDAR proportion. The SEM pictures show that the 100% TMDAR sample has the largest average grain size, and very few inter-grain pores, no inner-grain pores and the very narrow grain size distribution. On the other hand, the 100% CR-15 sample has the smallest average grain size, and the large grain size distribution. Many inter and inner grain pores remain in this sample. Except 100% TMDAR, all other full-sintered samples show a wide grain size distribution range. The reason lies on 1) the agglomerates in CR-15 and 2) high promoting grain growth elements: Na, K and Si in CR-15 powder, which are not evenly distributed in the system.
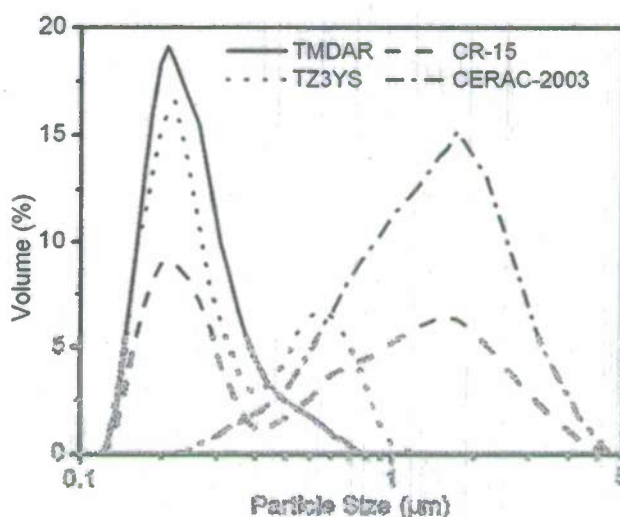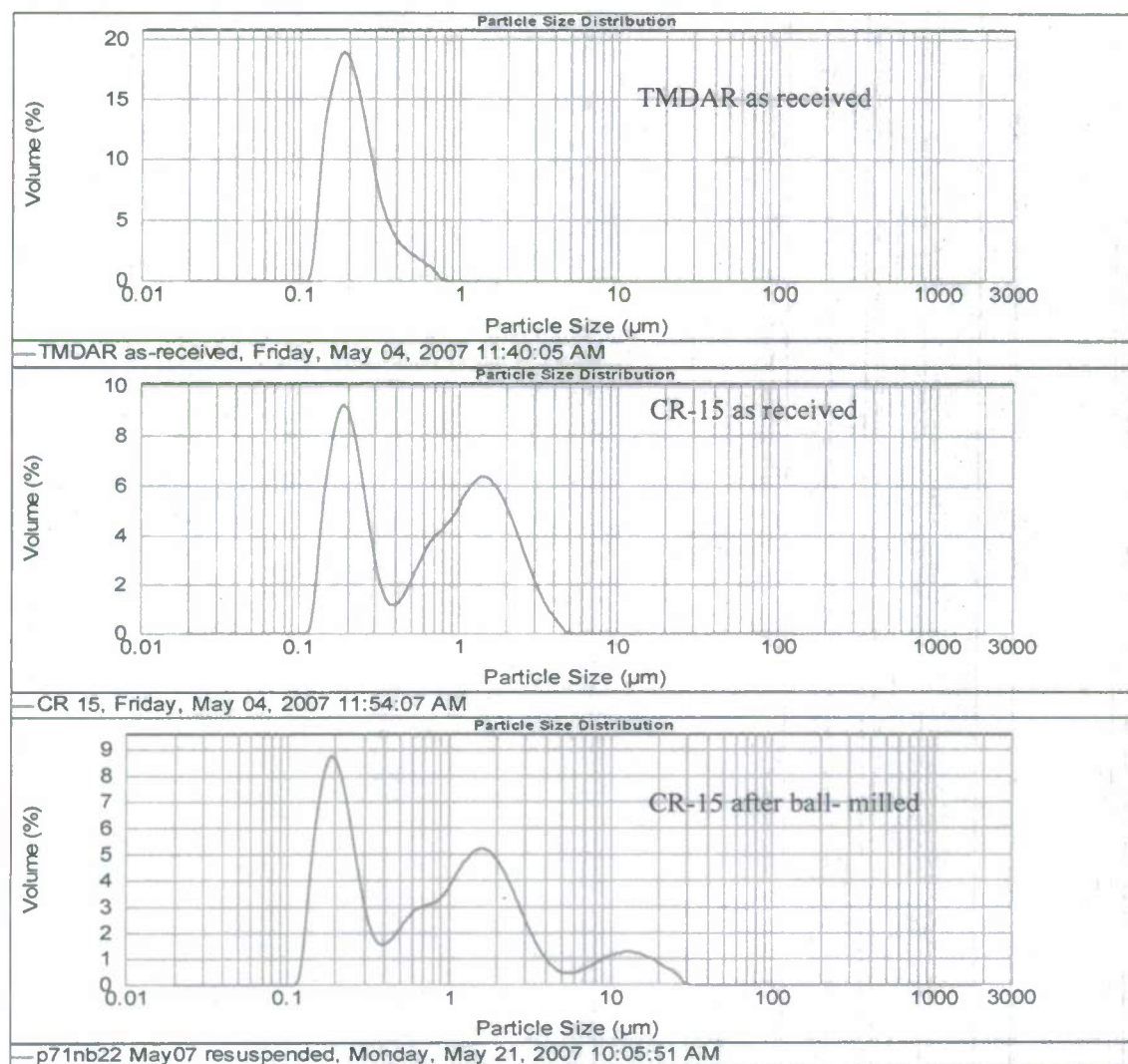
Figure 4.2: Powder Distributions of the Alumina Powders

Each curve on Figure 4.3 has a unique point for the maximum densification rate. The significance of this is that, before reaching this point, the porosity remains interconnected, and the grains do not grow [27]. Beyond the maximum densification point, the continuous pore network begins to collapse into isolated pores and grain grows rapidly [28]. With the increase in the proportion of TMDAR, the relative density at the maximum densification rate increases. The relationship between densification rate and relative density for TMDAR and CR-15 system shows a lower relative density and a larger grain size yielded a higher densification rate in the ascending part and lower densification rate in the descending part of the densification rate as seen in Figure 4.2. Our experiment observation matches the theoretical calculation presented in [29, 30]. Our results were attained based on the compaction under 200MPa pressure condition. The compaction of the powder is pressure-sensitive, yielding a variety of the green density and sintering curve [31, 32].
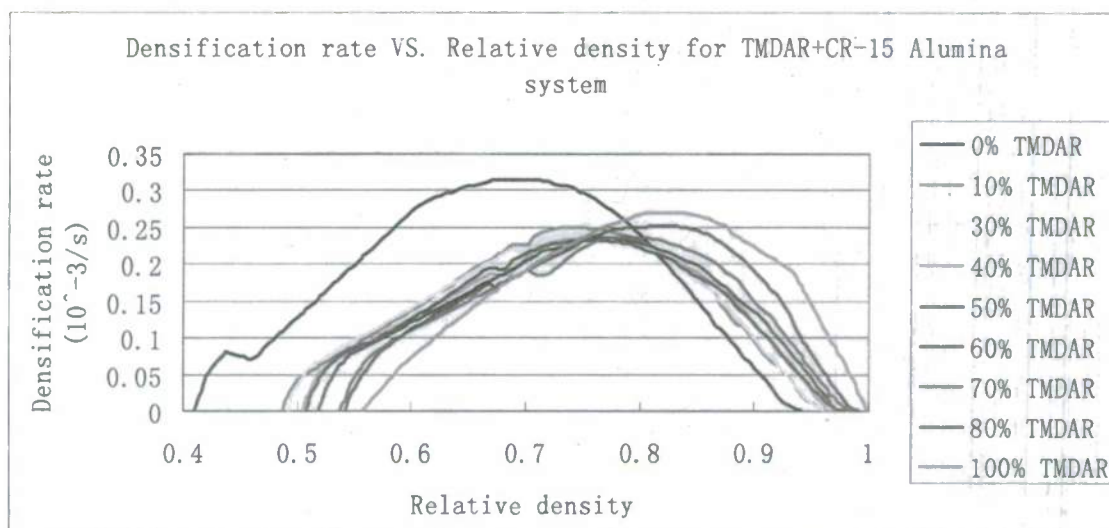
Figure 4.3: Densification Rate Curves

The experiment results for 100% TMDAR system under different pressure show that green density increases and densification rate decreases because of the less pore proportion. Figure 4.3 shows that the powder agglomeration influences the curve shape substantially. In the beginning of densification rate curves, the densification rate increases linearly. For the agglomerate-free TMDAR powder, one linear curve reached the maximum densification rate whereas in the powder with CR-15, the curves have to be described with two linear curves. The length of the first linear piece has direct relation with the proportion of the agglomerate. The length of the first linear part increases with the increase of TMDAR and reaching the peak at 60% TMDAR. This is believed to be the beginning; the small particles in the agglomerate and the other small-sized particles elsewhere dominate the sintering. Sintering of the agglomeration dominates the sintering behavior. More and lager the agglomeration, sintering requires more time, thus exhibiting a longer first linear curve. The slope of the densification curves is almost constant at the very beginning of sintering and independent of green density and agglomeration state. Lance et al. [28] has observed the similar results. However, Rahaman et al. [33] did not observe this phenomenon because he changed the load to achieve different initial relative densities.

Around 1100-1200 ℃, alumina has a γ-to-α phase change, which would cause to drop the densification rate, exhibiting a plateau in the densification rate curves. BSE (Back Scatter Electron) image (not shown here) on the 100% CR-15 sample attests to this phase change. In addition, the result under different temperature rates is presented. Becasue dl/ldT is the thermal conductivity, which is not influenced by heating rate. Similarly, dp/pdT in our experiment is also independent of the heating rate. Chu et al. [34] also obtain the same result. Finally, there is no plateau happens in the final stage. According to Lance et al. [28], that is due to the Abnormal Grain Growth (AGG). Our SEM images prove this conclusion. But the trace elements in the system give the wide grain size distribution like we analyzed before.
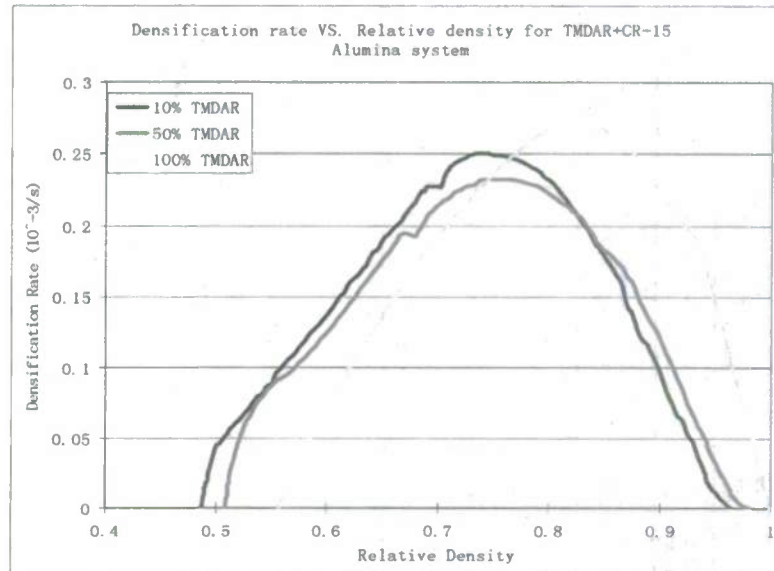
Figure 4.4: Densification Curves in relation to the Proportion of TMDAR.

To determine the constitutive models for the alumina powder, we need isothermal experiment data [35, 36]. In addition, we employed the stairway cycle method [37] shown in Figure 4.5. From stairway cycle experiment, we can get the relationship between densification rate and relative density shown in Figure 10. Hsueh [38] present a simple equation, which we consider to describe the sintering behavior of alumina.

$$\dot{\varepsilon}^s = \Omega(T)[D_\infty(T) - D]^n \qquad (4.1)$$

where $\dot{\varepsilon}^s$ is the densification rate, for our experiment, the relationship between densification rate and the displacement and displacement rate can be attained.

Figure 4.5: Evaluation of $D_\infty(T)$

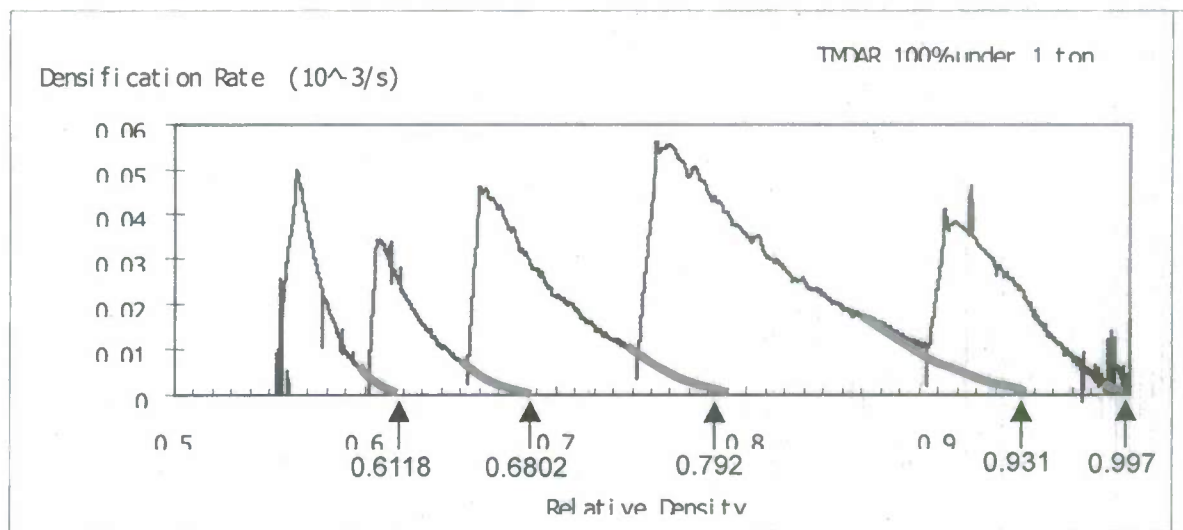To use Equation (4.1), we have to evaluate $D_\infty(T)$ which is the maximum relative density at temperature T by extending the isothermal curve to intersect with relative density axis. The intersection point is the $D_\infty(T)$. D is the relative density as shown in Figure 4.5. Thus, for any isothermal part, we can get the natural log curve like the left plot, and can get a linear approximation for each part. All the coefficient of $\ln(D_\infty-D)$ is close to 1.5, which is the exponent "n" in the densification formula. The intercepts of these equation give the $\ln(\Omega(T))$, then we can easily get the function $\Omega(T)$. $D_\infty(T)$ can fit into the hyperbolic tangent function [9].

4.3 Densification kinetics prediction model

The following equation for the sintering model for 100% TMDAR was attained.

$$\dot{\varepsilon}^s = [-1.138 \times 10^{-11}(T-100)^4 + 0.503408 \times 10^{-7}(T-100)^3 - 0.72765 \times 10^{-4}(T-100)^2 + 0.0319064(T-100) + 3.5792] \times \{\{0.2224\tanh[8.3785 \times 10^{-3}(T) - 9.4498]\} + 0.7776 - D\}^{1.5}$$

The comparison between calculation results and experiment data were excellent. Similarly, zirconia powders have been tested to attain the sintering models. Table 4.2 shows two distinct powders used in this study; TZ3YS (manufactured by Tosoh Corporation) and Cerac (manufactured by Cerac, Inc.). The major distinction is the absence of two distinct linear regions observed in alumina powders. The densification rate curve for TZ3YS is continuous nonlinear. Using the same technique, the sintering model for zirconia has been developed. The sintering model for 100%TZ3Ys, which apparently has excellent correlation with the experimental results, is

$$\dot{\varepsilon}^s = [1.00465 \times 10^{-9}(T-150)^4 + 5.83063 \times 10^{-6}(T-150)^3 - 1.26736 \times 10^{-2}(T-150)^2 + 12.2284(T-150) + 51384] \times \{\{0.2409\tanh[9.5305 \times 10^{-3}(T) - 12.259]\} + 0.7444 - D\}^{2.5}$$

Table 4.2: Zirconia Powder used

Powder name	TZ3YS	CERAC
Y_2O_3 (yttrium oxide)	6%	5.2%
ZrO_2 (Zirconia)	89%	94.8%
HfO_2 (Hafnium Oxide)	5%	0%
Average Particle Size (um)	0.59	1.23

The phenomenological models presented have few shortcomings:

1. The change due to phase change cannot be modeled accurately. Consequently, the simulation results vary compared to the experimental results around the phase change temperature

2. The models developed cannot be directly applied to the powder system where a reaction occurs during sintering (such as Mullite). This may be addressed by piece by piece calculation.

5. ZrO_2-Al_2O_3 STEPWISE FGM

Cracks and camber are prevalent when co-sintering multi-layered Functionally Graded Material (FGM) due to the residual stress caused by the mismatches in thermal expansion and sintering between successive layers. This section describes a novel processing technique to relieve the residual stress in such co-sintering process. Thus during operation the process-induced residual stress will not jeopardize the structural integrity of the core. The effectiveness of the proposed technique was demonstrated by fabricating a three-layered Al_2O_3/ZrO_2 FGM. Various processing parameters, such as the powder characteristics, compaction load, interface profile, and temperature ramp/soak profiles, were varied in order to determine the optimum parameters for eliminating cracks and decreasing camber. The optimum processing parameters include low compaction load, higher ramp rate, a proper mixing of multiple powders with distinct powder characteristics and the modification of interface profile in producing undamaged and undistorted samples. In addition, the thermomechanical analysis (TMA) on various powder mixtures with the determined optimized parameters was carried out, which indicates: 1) the shrinkage rate–sintering temperature curves of each layer are almost identical and 2) the shape of the densification rate-relative density curves are very similar, yielding a common term in the phenomenological constitutive models of all three layers.

In the series of experiments, two alumina powders and two zirconia powders were used. All the powders feature submicron particle sizes. The detailed starting powder characteristics are summarized in Table 5.1. The alumina powders include TMDAR (Taimei Chemical CO., LTD., Japan) and CR-15 (Baikowski Ind. Corp., U.S.A.). Both were high-purity and undoped. The two zirconia powders used were TZ3YS (Tosoh Co., Japan) and CERAC-2003 (CERAC Inc., U.S.A.), both of which were partially stabilized with 3% Y2O3 in mass. The particle size distribution for each grade was measured by the Malvern Mastersizer 2000 and the results are presented in Fig. 5.1.

Table 5.1: Powder Characteristics

Material	Powder name	α-phase content	Mean particle size (μm)	Chemical analysis (ppm)					
				Na	K	Fe	Ca	Si	Mg
Alumina	TMDAR	100%	0.17	4	2	5	3	3	1
	CR-15	90%	0.42	13	22	2	3	13	1
Zirconia	TZ3YS		0.54	Stabilized by 3% Y_2O_3					
	CERAC-2003		1.23						

Figure 5.1 clearly shows that both TMDAR powder and CERAC-2003 powder have a single-peak powder size distribution profile, while the plots of CR-15 and TZ3YS powder display a dual-peak profile. The second peak of these two plots is from the agglomerates present in the CR-15 and TZ3YS powder. The micrographs of the four raw powders show that the TMDAR and CERAC-2003 are almost agglomerate-free, but the CR-15 and TZ3YS

powders feature many agglomerates. Various proportions of the four raw powders were mixed using 12mm diameter alumina and/or zirconia mixing media in a jar mill (U.S. Stoneware 764AVM, U.S.A.) for 48 hours. The powder mixtures were compacted in a single-action die and sintered to construct FGM specimens featuring three layers of equal thickness. The top layer is 100% zirconia (denoted as layer Z), the bottom layer is 100% alumina (layer A), and the middle layer is a mixture of 50% by volume of the alumina powder and zirconia powder (layer M). The interface profiles between the layers can be controlled, which will be discussed in

Figure5.1. Particle size distribution profile of powders used in this study.

section 3.3. In order to ensure that each layer has the same volume, the mass of alumina and zirconia to be present in each layer needed to be calculated using the theoretical densities, which are 6.05g/cm3 for ZrO_2 and 3.87–3.98g/cm3 for Al_2O_3 layer depending on the content of CR-15 powder. . The mass ratio for each layer can be described
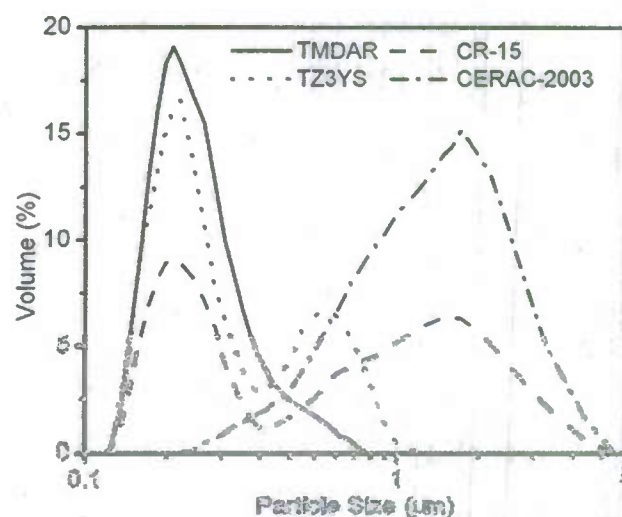
as $m_A : m_M : m_Z \approx 1 : 1.24 : 1.478$.

Naturally, in the powder mixture of layer M, the mass ratio of alumina to zirconia is nearly 1:1.478. The load to compact powder stacks was in the range of 60 to 210MPa. The green samples were of 22.02mm diameter and had a height between 4.2 and 4.75mm depending on the compaction load used. Green compacts were sintered in air at 1475°C. Several different ramp/soak sintering cycles were used in order to determine the influence of heating/cooling rate on the sintering process. The real time sintering testing was performed using the high temperature dilatometer (Setaram 95, France) with argon gas providing a protective environment. The green samples for real time sinter test were 7.94mm in both diameter and height. The volume of the full-sintered pieces was measured in water by Archimedes' principle. To attain clear micrographs, the full-sintered samples were polished using polisher (Abramin, Denmark) and thermal-etched in a box furnace at 1400°C. The microstructure was observed by Scanning Electron Microscopy (JEOL 6400V, Japan).

5.1 The influence of the powder combination

The content of powder mixture dictates its compactability and sinterability, ultimately changing the diameter of the final product. Figure 5.2 shows the variation of final diameter with respect to the powder mixtures of alumina and zirconia. The two characteristics of the powder mixtures that influenced the shrinkage of the green compact were the packing density of contents and the particle size distribution. Therefore, with a higher proportion of more

compactable powders and the optimum particle size distribution, the initial green compacts will attain a higher green density under the same compaction load. They thus shrink less, resulting in a larger final diameter.

When considering the alumina powders, TMDAR has a much higher compactibility than CR-15. This means that powder compacts containing a higher proportion of TMDAR lead to a larger final diameter under the same load. It is seen from Figure 5.2(a) that the final diameter of alumina increased significantly when the proportion of TMDAR was raised from 0% to 10%. As the proportion of TMDAR increases further, the final diameter increased almost linearly.

In the zirconia system, the situation is quite different since the pure CERAC-2003 and TZ3YS powder have a very similar compactibility. Thus the particle size distribution will be the main factor in determining the final diameter. Table 5.1 shows that CERAC-2003 has a much larger average particle size than TZ3YS. It follows that, in some combination of these two powders, the small TZ3YS particles will fill in the interstitial spaces among the larger CERAC-2003 particles. Powder combinations meeting this criterion have a

a

b

Figure 5.2. The relationship between the final diameters and the percentage of a) CR-15 in alumina system and b) CERAC-2003 in Zirconia system under varying compaction load.

higher compactibility than either of the pure powders. As can be seen in Figure 5.2(b), when the proportion of CERAC-2003 was between 30 and 80% in the zirconia powder system, the final diameter of full-sintered pieces was much larger than others.

To achieve the flatness in the FGM specimen (no significant camber), the essential requirement is that the final diameter of each layer should remain at a similar value. This does not guarantee, however, the survivability of the FGM specimen during co-sintering, since the final diameter of each layer may be the same but the shrinkage rate at each layer during the co-sintering process can be substantially different. Definitely, a large difference in the final diameter between two layers induces residual stress, resulting in either cracks or camber. Comparing Figure 5.1 (a) and (b), the final diameters of alumina are most often larger than
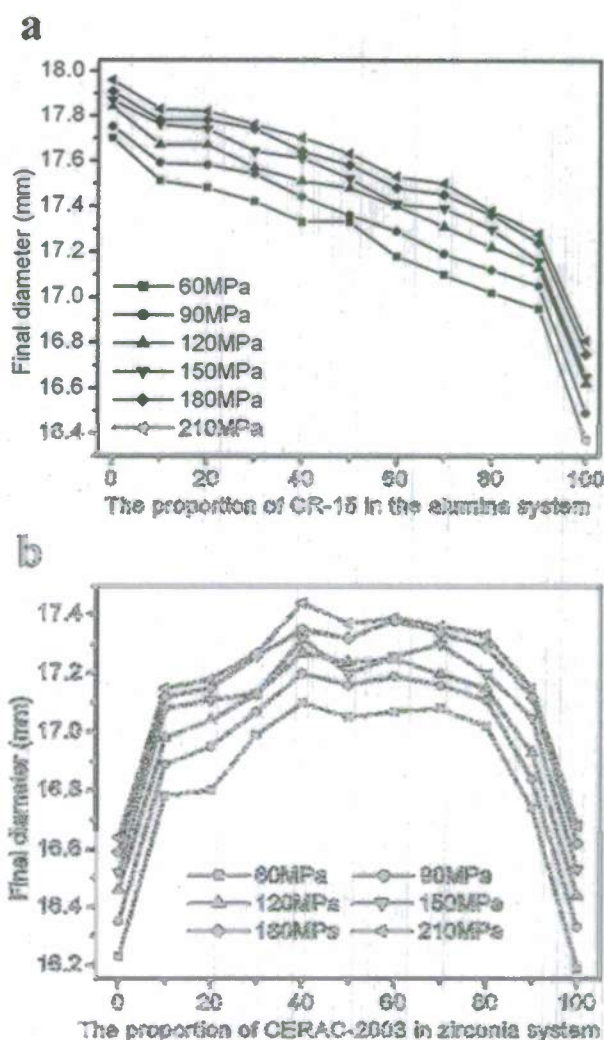
those of zirconia compacted at a same load; only when the proportion of CR-15 in alumina system is higher than 80%, it was possible to achieve similar dimensions in the alumina and zirconia layers.

Since the powder combination of 40% CERAC-2003 and 60% TZ3YS yields the largest final diameter for zirconia layer, we fixed this proportion for layer Z in this study. The volume proportion of CR-15 in layer A was then varied from 82% to 100%. The proportions of each powder used in layer M will be the same as those used in the other two layers on the first try, but the excellent compactibility of TMDAR may lead to an adjustment of its proportion. After several tries, we found that for layer A, the best powder combination to be 94% CR-15 and 6% TMDAR and for layer M, the optimum mixture to be 46% CR-15, 4% TMDAR, and 20% CERAC-2003, 30% TZ3YS in volume.

5.2 The influence of the compaction load

The compaction load also affects the final diameter. Figure 5.2 also depicts this relationship. For any given powder combination, the final diameter and the compaction load are can be seen to be directly proportional. As the compaction load increases, the particles in each specimen pack together more tightly, resulting in an increase in the green density [39]. This decreases the shrinkage, ultimately leading to a larger diameter on the fully sintered samples. However, for a material system under varying compaction loads, the plots seem to display a 'parallel characteristic', suggesting that the change in the compaction load does not impact the relation between the final diameter and the content of the powder mixture. As the compaction load increases, the normal stress being exerted on the powder by the die will increase. Therefore, in the ejection step, there is a larger friction force between the die and the powder. The increase in friction raises the possibility of camber or cracks. In addition, beyond a critical load the yield surface of ceramic powders move out to the shear failure surface [40]. The particles slide against each other, resulting in micro-cracks, which may eventually lead to a crack in the sample.

In this study, we found that the change in compaction load resulted in various damage characteristics in the sample. Thus, it is reasonable to consider that a low compaction load is preferable in order to achieve undamaged and undistorted FGM samples. However, the use of a compaction load lower than 40MPa causes the green bodies to be too weak. Acompaction load of 60MPa was chosento be the optimized compaction load.

5.3 The influence of the interface profile

In the processing of multi-layered FGMs, typically a free and flat interface (natural interface) is used between two successive layers. However, this study finds that with the natural interfaces of the Al_2O_3/ZrO_2 FGM sample, cracks were formed between layer A and layer M despite of no apparent camber on the sample. This crack formation necessitated the investigation into using more complex interfaces. Two additional interface profiles were investigated in this study: smooth and occlusive. The smooth profile is obtained by lightly rotating the regular flat punch without any pressure. The smooth interface has a smaller

interface area than the natural interface. The occlusive interface profile, so named because it resembles the way in which the cusps of molars from the upper and lower jaw fit together, yields an increase in the interface area. This profile will be obtained by pressing the lower powder layer with a punch featuring a jagged surface and pouring the powder for the subsequent layer.

Considering the structure of our FGM sample, each interface requires its distinct profile to prevent the formation of cracks. The interfacial crack between the layers A and M indicates that the bonding between A and M was weaker. The interlock structure of the occlusive interface would increase the bonding between these two layers. In addition, the occlusive interface creates a quasi-continuous intergradation, which provides a more continuous material properties transition between these two layers when compared to the other two interface profiles. At the same time, the interface between M and Z was much stronger as no interfacial crack has been detected. For our powder systems, we found that only the combination of a smooth interface between the layers M and Z and an occlusive one between the layers A and M prevents the formation of cracks.

5.4 The influence of the ramp/soak sintering cycle

The mixing proportions of powder have been determined in order to achieve nearly equal final diameters. However, the transient diameter change during the sintering process is also important to yield samples without camber and cracks. Figure 5.3 shows the change in the shrinkage rate of powder mixture for layer A and layer Z under an isothermal experiment at 1250°C. It is clear that the shrinkage rate of layer Z is higher than that of layer A at this temperature. In fact, this conclusion is suitable for the whole sintering temperature range we used. This sintering mismatch contributes the most important factor in creating cracks or

Figure 5.3:. Shrinkage Rate Difference for layer A and layer Z under an isothermal sintering experiment at 1250°C. (dh(t) is the height changing rate and h(t) is the height of

camber as mentioned above. However, considering that alumina has much higher thermal conductivity than zirconia [41,42], with a faster ramp rate, alumina can be heated up more quickly and may catch up to the shrinkage of zirconia in the co-sintering process. This results in a reduction in the transient mismatch of shrinkage between different layers. From our observation, if the previously determined optimal system of powder mixtures is sintered with a lower ramp rate (less than 7°C/min), cracks formed on the surface of layer A. Final samples were free of cracks and camber if the ramp rate was higher than 10°C/min and a two-hour
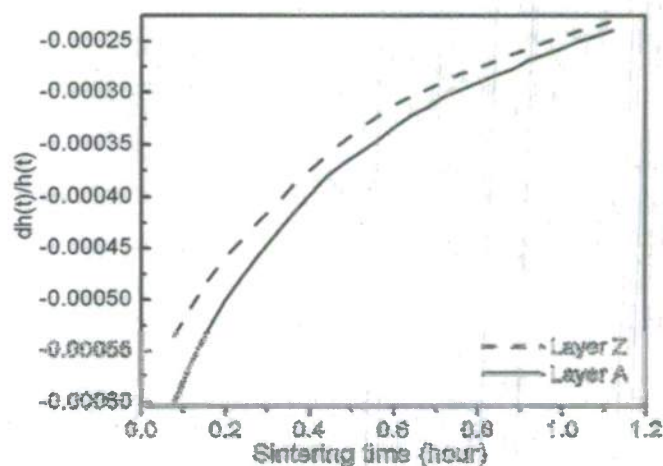
soak interval was used. However, considering the low thermal conductivity of ceramics, the ramp rate cannot be set too high. This would cause a large temperature difference within a sample and may create a condition for cracks [43].

Because of the difference in the CTE between fully sintered zirconia and alumina layers, a lower cooling rate was preferred to avoid cracks, since the residual stresses can be relaxed in the initial period of cooling [43]. In our experiments, the cooling rate of 4°C/min is low enough to prevent cracks caused by CTE mismatch and the final optimized ramp/soak sintering cycle was determined.

5.5 Shrinkage rate – sintering temperature curves of chosen powders under optimized condition

Table 5.2 summarizes the discussion in earlier sections and provides the optimal parameters to yield undistorted, flat three-layered Al_2O_3/ZrO_2 FGM samples without cracks. The shrinkage rate-sintering temperature plots of the three chosen powder mixtures under the optimal processing parameters. All three powder mixtures begin sintering at about 1050°C and that they have very similar transient shrinkage from that point onward. The similarity of shrinkage rate for those chosen powder mixtures ensures that no significant dimensional mismatch could occur at any time during sintering, thus reducing the possibility to form cracks or camber. Torrecillas et al. [44] studied an FGM system featuring zircon and molybdenum, stating that if the transient shrinkage state is almost the same for each layer, then the final fully-sintered specimen is flat and free of residual stress. The present work verifies their conclusion.

5.6 Densification rate – relative density curves of chosen powders under optimized condition

Another commonly used curve to describe the sintering kinetics of ceramics is densification rate-relative density curve. The relative density D is the ratio of the mass density of the sample to the theoretical density of the corresponding powder mixture. And the densification rate is defined as:

$$\dot{\varepsilon}^s(T) = \frac{\partial \rho}{\rho \, \partial t} = \frac{\dot{D}(T)}{D(T)} \tag{5.2}$$

Table 5.2: A summary of optimized experimental conditions for a 3-layered Al_2O_3/ZrO_2 FGM.

	Layer Z	60% TZ3YS, 40%CERAC-2003
	Interface Z/M	Smooth
Structure	Layer M	20% CERAC-2003, 30% TZ3YS 46% CR-15, 4% TMDAR
	Interface M/A	Occlusive
	Layer A	94% CR-15, 6%TMDAR
Compaction load		60 MPa
Rate of temperature change		10°C/min for heating, 4°C/min for cooling

Since the dilatometer only can measure the length change in one direction, to calculate the densification rate based on the results of dilatometer, Lance et al. [28] defined an anisotropic shrinkage factor α:

$$\alpha = \frac{(\varphi_f - \varphi_O)L_O}{(L_f - L_O)\varphi_O} \tag{5.3}$$

where Lo and Lf are the initial and final height of the specimen, and φo and φf are the initial and the final mean diameter of the specimen. For all of our experimental results, α was almost 1 (>0.991). It is therefore reasonable to consider the sintering process for our samples to be a self-similar (isotropic) one. Thus, with the 1:1 height to diameter ratio, the temperature dependent relative density and the strain rate can be calculated.

The densification rate-relative density curves for the three chosen powder mixtures under the optimal parameters were obtained (Figure 5.4). The shape of the three curves is very similar. One obvious difference is located around $0.22 \cdot 10^{-3}$/s densification rate in the ascending portion. The corresponding sintering temperature range is 1150-1200°C. There is a plateau for layer A and a drop in slope for layer M, but there is no noticeable change for layer Z near this region. The change in densification rate for layers A and M is a result of γ- to α-phase transition of alumina [45] since 10% γ-phase alumina is present in CR-15.

Figure 5.4. The densification rate-relative density curves for the three chosen powder mixtures under optimized experimental

However, since layer Z does not contain CR-15, there is no plateau or abrupt slope change in its densification rate curve. Due to the similarity of the densification rate-relative density curves shown in Fig. 10, it is intuitive to investigate and compare the constitutive model describing these three curves. Based on Section 4, the resulting constitutive models were compared.The errors between the experimental data and the calculated results are less than ±6%. It should also be pointed out that the simulation result from the phenomenological constitutive model does not display the plateau that occurs in conjunction with the phase change.█
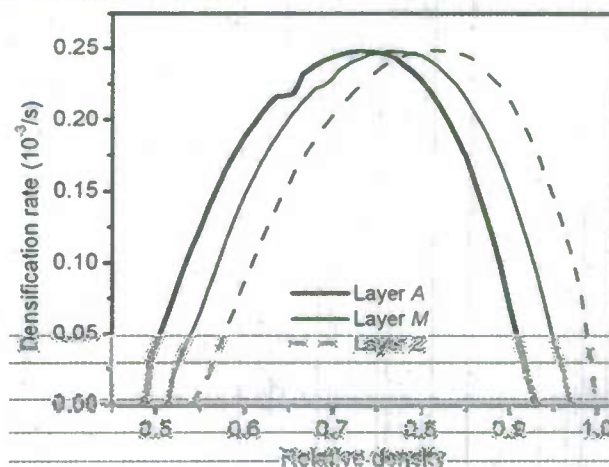
6. ZrW$_2$O$_8$ AND ZrW$_2$O$_8$-ZrO$_2$ COMPOSITES: IN-SITU REACTION AND PHYSICAL PROPERTIES

By the in-situ synthesis of WO$_3$ and ZrO$_2$ in a particular mass ratio, ZrW$_2$O$_8$, a negative Coefficient of Thermal Expansion (CTE) material, was fabricated. By increasing the proportion

of the ZrO_2, the product was changed to a wide variety of ZrW_2O_8/ZrO_2 composites. The temperature dependences of the CTE and Young's modulus of these materials were measured and the experimental data were compared with the predictions from several models. Among these models, the modified Mori-Tanaka method offers an excellent correlation to the experimental values of Young's modulus, while the Levin model produces CTE values that are the most similar to the values from the CTE testing. This was the first time the micromechanics models were applied to predict the CTE of composite materials containing a negative CTE material. The ZrW_2O_8/ZrO_2 composite with a designed CTE can be fabricated and utilized to meet a special thermal requirement in many industrial applications.

The ZrW_2O_8/ZrO_2 composite with a desirable CTE can be fabricated to meet particular thermal expansion requirements for a given industrial application. For example, the thermal expansion of a composite can be designed to match with the thermal expansion of other adjacent mechanical or electronics components. Specifically, a ZrW_2O_8/ZrO_2 composite with near-zero CTE can be used as the ceramic substrate of optical fiber Bragg gratings in order to keep the constant dimension under the temperature-changing environment.

Table 6.1 summarizes the three raw powders used in this study. These powders were mixed in varying proportions using 12mm diameter zirconia media in a mixing jar mill (U.S. Stoneware 764AVM, U.S.A.) for 48 hours. The powder mixtures were compacted in a single-action die under the load producing 80MPa compaction pressure. The green samples for CTE testing were cylindrical with 7.94mm diameter and 6mm height while the green samples for Young's modulus testing were rectangular parallelepipeds whose dimension is 16.5mm×5.05mm×3.5mm. Green compacts were sintered in the furnace (Carbolite-HTF1700, UK) under the atmospheric condition in a covered platinum crucible, which can decrease the sublimation of WO_3 at temperatures above 800°C [46]. The ramp/soak path in sintering will be described in Section 6.1. The volume of each fully-sintered sample was measured in water using Archimedes' principle, which was then used to calculate the relative densities.

Table 6.1: Mean features of raw powders used in this study

Name	Material	Mean particle size (μm)	Manufacturer
W-Fluka	WO_3	8.22	Sigma-Aldrich, U.S.A.
TMDAR	Al_2O_3	0.17	Taimei Chemical CO., LTD., Japan
CERAC-2003*	ZrO_2	1.23	CERAC Inc., U.S.A.

* Stabilized by 3w% Y_2O_3

Before testing CTE and Young's modulus, the samples were heat-treated (3°C/min for both heating and cooling cycles, and soaking for 60 minutes at 300°C) to cure microcracks induced by the quenching process [47]. The CTE and Young's modulus of the sintered samples were measured using the TMA with the heating and cooling rates of 1°C/min in an argon gas environment. Three samples produced for each material were tested for CTE and Young's modulus. The CTE variation is less than 5% and the maximum discrepancy in the

Young's modulus data is 6% in the three samples. Therefore, we considered that the CTE and Young's modulus test results for each material are consistent and each reported value is the average of the corresponding results of three samples. The sintered samples were then polished (Abramin, Denmark) and thermal etched in the furnace at 600°C for the microstructure observation. The microstructure of each sample was observed using Scanning Electron Microscopy (JEOL 6400V, Japan).

6.1 Fabrication of ZrW_2O_8

From the WO_3 and ZrO_2 bi-Phase diagram [48], one can find that ZrW_2O_8 can only exist at temperatures above 1110°C, and the compound is only stable between 1110 and 1260°C. Therefore, in the processing of ZrW_2O_8 substrate, the final soaking temperature must be above 1110°C and an appropriate quenching step is necessary to prevent the decomposition of ZrW_2O_8. Based on these two requirements, the ramp/soak profile shown in Figure 6.1 was used to produce ZrW_2O_8 from a 2:1 stoichiometric ratio of WO_3 and ZrO_2 powder mixture (mass ratio is mWO_3: $mZrO_2$ =1:0.266). The heating rate is 5°C/min and the soaking temperature is set at 1190°C. The balanced reaction can be expressed as follows:

$$ZrO_2 + 2WO_3 \rightarrow ZrW_2O_8 \qquad (6.1)$$

After quenching in open air, the surfaces of the samples featured small cracks. These microcracks disappeared completely after the cure treatment cycle mentioned above.

The temperature dependence of the ZrW_2O_8's CTE was measured, and this relationship is shown in Figure 6.2. Also shown is the CTE-temperature relationship of partially sintered CERAC-2003 utilizing the ramp/soak path. These two ceramics are the components of the composites presented here. As expected, the CTE of ZrW_2O_8 is negative and uniform for a wide range of temperature except around 160°C, where a sharp change occurs due to α-to-β phase
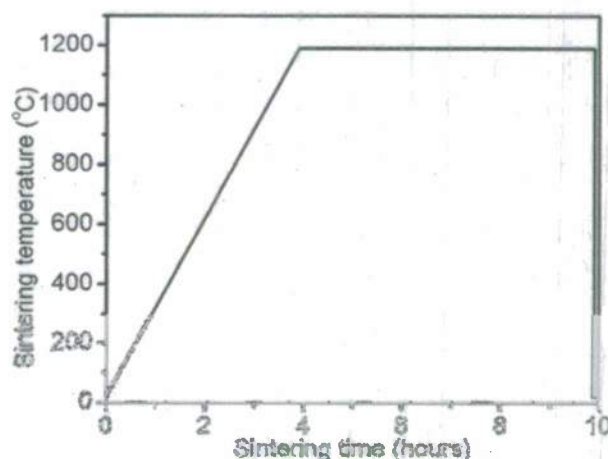

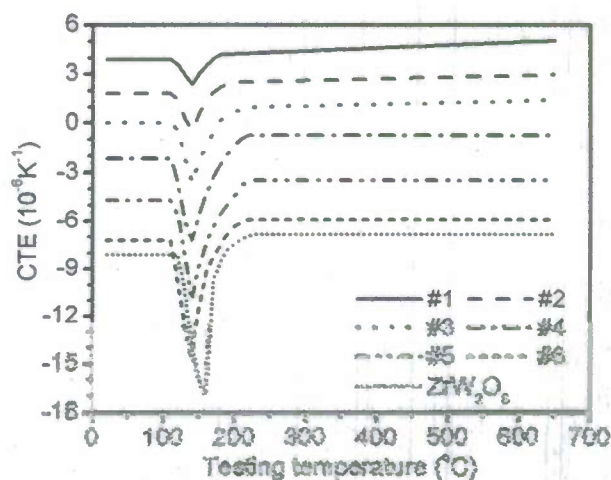Figure 6.1: The ramp/soak path used for producing ZrW_2O_8.

Figure 6.2: The temperature dependent CTEs of the various ZrW_2O_8/ZrO_2 composite samples.

transition [5]. The CTE of the ZrW_2O_8 at room temperature was found to be $-8.1 \times 10\text{-}6K\text{-}1$, a result that matches the report of Mary et al. [5]. The CTE of the partially sintered CEREAC-2003 is $8.6 \times 10\text{-}6K\text{-}1$ at room temperature.

6.2 ZrW2O8/ZrO2 Composites and the CTE-temperature relationship

With the ramp/soak path shown in Figure 6.1 and a higher proportion of ZrO_2, a ZrW_2O_8/ZrO_2 composite instead of ZrW_2O_3 can be fabricated. Thus, by varying the ratio of $WO3$ to ZrO_2, the resulting composites feature varying ratio between ZrW_2O_8 and ZrO_2. Table 2 shows several WO_3/ZrO_2 mass ratios used in this study and the corresponding resultant ZrW_2O_8/ZrO_2 volume ratios in the sintered samples. The temperature-dependent CTE value of each sintered sample is shown in Figure 6.2. As shown, both Samples 1 and 2 feature positive CTEs, Samples 4-6 exhibit negative CTEs, and the CTE of Sample 3 is nearly zero. Figure 6.2 shows that the CTE-temperature curves of the composites feature a shape that is very similar to that of pure ZrW_2O_8. However, the peak caused by phase transition occurs at a lower temperature for the composites. This "peak shift" is possibly a result of phase transition from α-ZrW_2O_8 (low pressure phase) to γ-ZrW_2O_8 (high pressure phase) [49] due to the thermal stress induced by the CTE mismatch between ZrO_2 and ZrW_2O_8.

Table 6.2. The WO_3/ZrO_2 mass ratios of various green samples and the corresponding resultant ZrW_2O_8/ZrO_2 volume ratios in the sintered samples.

#	WO_3/ZrO_2 mass ratio in reactant powder	ZrW_2O_8/ZrO_2 volume ratios in the sintered sample	Final relative density
1	0.159:1	20:80	77%
2	0.264:1	30:70	79%
3	0.38:1	38.9:61.1	80%
4	0.593:1	51.5:48.5	82%
5	1.096:1	70:30	83%
6	2.307:1	90:10	84%

6.3 CTE-phase volume ratio relationship

The relationship between the CTEs of various samples and the corresponding volume fractions of ZrW_2O_8 for both room temperature and 500oC testing conditions is plotted in Fig. 6.3.a and 6.3.b, respectively. It can be observed that the CTE values continuously decrease as the volume fraction of ZrW_2O_8 increases in the composites. For the zero CTE ZrW_2O_8/ZrO_2 composite, the volume fraction of ZrW_2O_8 in the final product is about 38.9% (Sample 3). To predict the properties, the ROM is the simplest method to calculate the effective CTE of a composite. By using the CTE testing results of ZrW_2O_8 and ZrO_2, the effective CTEs of ZrW_2O_8/ZrO_2 composites were calculated based on the ROM and presented in Figure 6.3. Large discrepancies exist between the experimental results and the calculated values from the ROM for both room temperature and 500°C testing conditions. In fact, the ROM predicts

that Sample 4 has a room temperature CTE of nearly zero, but the experimental data showed its CTE to be $-2.14 \times 10^{-6} K^{-1}$. This discrepancy is due to the porosity of the resulting composites. At the same time, the ROM to predict affective CTE does not include the elastic constants that account for the thermal stress influence between ZrO_2 and ZrW_2O_8.
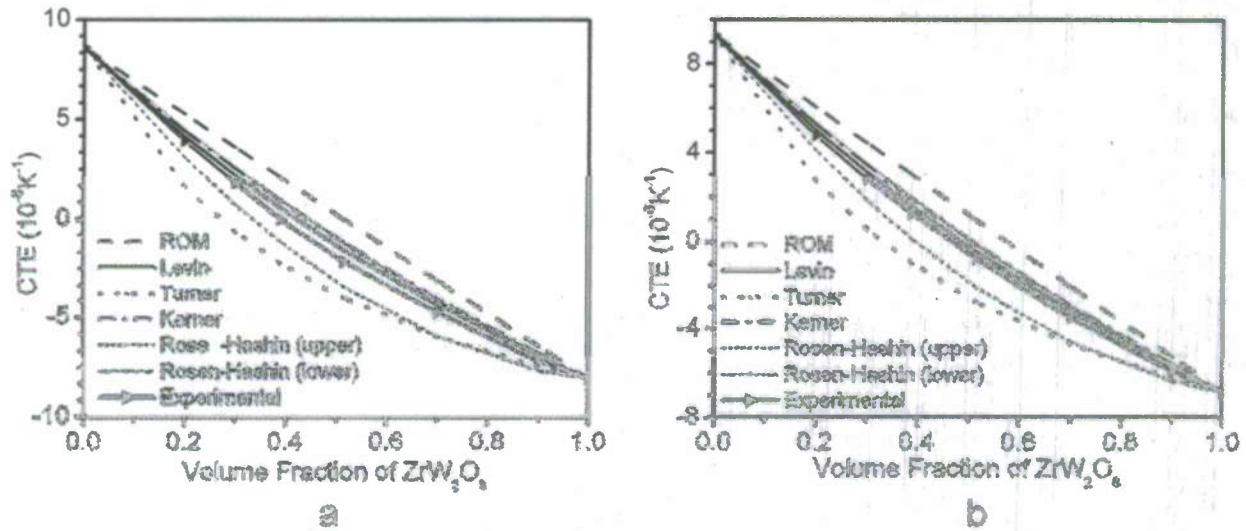

Figure 6.3. The CTEs of the ZrW_2O_8/ZrO_2 composite samples and corresponding calculated values from several prediction models at a) room temperature and b) 500°C.

The calculated CTE as a function of v% of ZrW_2O_8 results from various methods including Rule of Mixture, Turner [50], Kerner [51], Rosen-Hashin [52] and Levin [53], and also are shown in Figure 6.3, which take into account the elastic constants in the calculation of CTEs. The values of various elastic constants of ZrW_2O_8 and ZrO_2 necessary for the CTE calculation are calculated based on the experimental data of Young's modulus and the assumed Poisson's ratio. Among these, the Levin model produces CTE values that are the most similar to the experimental data. The maximum error of Levin model was found to be less than 8%. By studying the series of Al_2O_3/NiAl composites, Hsieh et al. [54] concluded "the Kerner and Turner models can be used as the upper and lower bounds for the CTE of two-phase materials, respectively." This conclusion also matches the results from our ZrW_2O_8/ZrO_2 composites. Another interesting finding is that the upper boundary predicted by the Rosen-Hashin Bounds model [52] almost superimposes on the curve form Kerner model [50] for the ZrW_2O_8/ZrO_2 composites.

All of the ZrW_2O_8/ZrO_2 composites maintained their initial cylindrical shape, with final diameter and height around 7.35mm and 5.57mm, respectively, and they featured final relative densities in the 77-84% range (see Table 2). This low density persists mainly because ZrO_2 has not been fully sintered by the ramp/soak path shown in Figure 6.1. In the representative micrograph of the composite, the large particles surrounded by small ZrO_2 particles are ZrW_2O_8. The abundance of pores remaining between the ZrO_2 particles is due to the fact that ZrO_2 is far from fully sintered. In addition, cracks are observed to exist between

ZrO_2 and ZrW_2O_8 grains, resulting from the considerable difference in CTEs for these two component materials. These cracks also contribute to the low final density.

6.4. Young's modulus testing

The TMA unit offers a facility to measure Young's modulus of materials using the three-point bending method. After sintering and polishing, the samples used in Young's modulus testing are rectangular parallelepipeds (cuboids) with edge lengths 12.6mm, 4.2mm and 2.5mm. The temperature dependent Young's moduli of the fabricated composites as well as that of ZrW_2O_8 and ZrO_2 are obtained. Since the ZrO_2 in the composites is processed by the ramp/soak path shown in Fig. 1, the CERAC-2003 for Young's modulus testing was also partially sintered by the same ramp/soak path. Microcracks formed in the ZrO_2 samples due to the quenching process. The highest testing temperature was set as 650°C in order to avoid the decomposition of ZrW_2O_8. The room temperature Young's modulus of pure ZrW_2O_8 was found to be 4.31GPa, which nearly matches the value of 4.22GPa reported by Chen et al. [47]. However, these values quite different from the single crystal value of 88.3GPa reported by Drymiotis et al. [55]. Since the ZrO_2 sample was only partially sintered and contains microcracks, its Young's modulus is much lower than that of a fully-sintered sample (~200GPa) and it does not feature a large decrease from 100 to 400°C, which is typical for fully-sintered ZrO_2 [56]. As happened with CTEs, the Young's moduli of the composites and the ZrW_2O_8 feature a value change around 160°C due to the α to βphase transition.

From the reports of Drymiotis et al. [56] and Holcome et al. [57], we assumed the Poison's ratio is 0.3 for both ZrO_2 and ZrW_2O_8. Therefore, with the Young's modulus values for ZrW2O8 and partially sintered ZrO_2, we calculated the elastic constants and the Young's moduli of ZrW_2O_8/ZrO_2 composites by the Mori-Tanaka method. These results are shown in Fig. 9 along with the experimental Young's modulus of the composites. It can be seen that the experimental data lies between the two curves predicted by the Mori-Tanaka method. Based on the observation of microstructures of the composites, we used four different continuity values, listed in Table 3, for Kwon and Dharan [58] revised Mori-Tanaka method and represented on the curve in Figure 6.4. As can be seen, the revised Mori-Tanaka method shows a much better fit with experimental data. The maximum error of Mori-Tanaka method revised by Kwon and Dharan [58] was found to be only 4%.

6.5 Final Density improvement

If one adds a small amount of Al_2O_3 into the powder system, a very complex chemical reaction happens when temperature is above 1100°C:

$$ZrO_2+WO_3+Al_2O_3 \rightarrow ZrW_2O_8+Al_2(WO_4)_3+ZrO_2+Al_2O_3 \qquad (11)$$
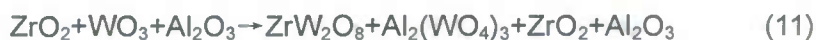
Due to the melting point of $Al_2(WO_4)_3$ at 1135°C [59], a liquid phase exists at the soaking temperature of 1190°C. The presence of this liquid will promote the densification kinetics, resulting in the improved final relative density.

The addition of 0.07w% Al_2O_3 caused the final relative density to increase from 80 to 90%. Furthermore, the minute amount of TMDAR allowed the samples to maintain their cylindrical shape.
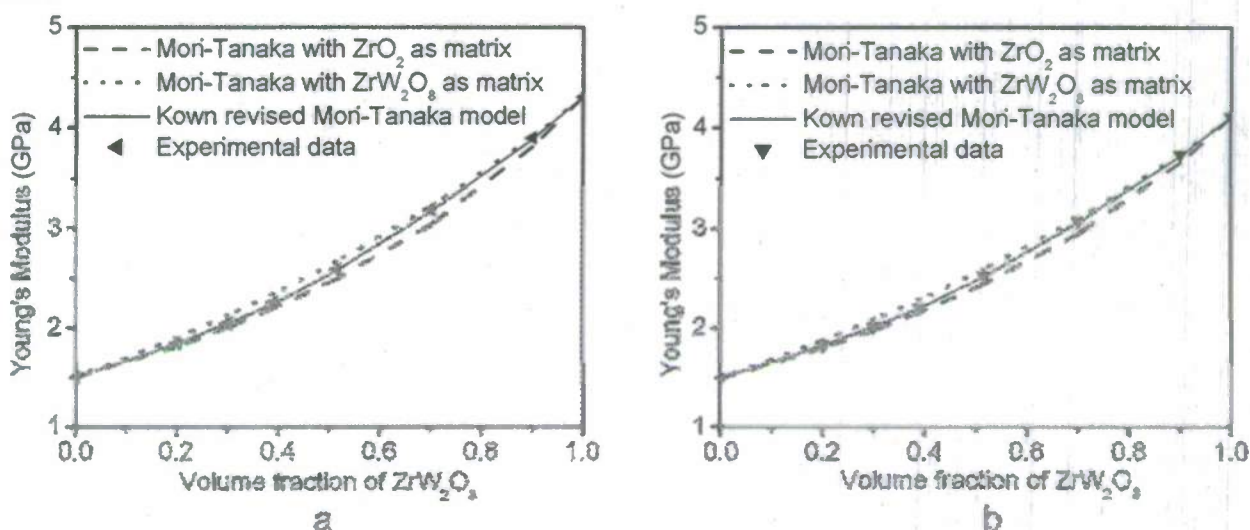

Figure 6.4: The calculated Young's modulus of ZrW_2O_8/ZrO_2 composites by Mori-Tanaka model and the experimental measurement of composites at a) room temperature, b) 500°C.

7. STRUCTURE DESIGN OF PERSPIRABLE SKIN BY FEA

In this material system, several ZrW_2O_8 pegs are shrink-fit into the Reinforced Carbon-Carbon composite (RCC) skin. At working conditions, a gap or interference forms between the two materials and the compressed gas within the vehicle can blow out through the gap. The atmospheric air, rather than contributing to the frictional heat between air and skin, is mixed with the cold compressed air over the surface. Due to the nonlinear thermoelastic properties within the operating temperatures, Finite Element Analysis was used to design the geometry of the ZrW_2O_8 pegs and the best fiber arrangement of the RCC for this material system. The geometry of the peg with a larger radius at the top surface and a smaller radius at the bottom part ensures the secure contact of two materials at the working condition. The design with the frustum of a cone shaped top offered a better and shorter route for the coolant gas to be passed. The best type of RCC is found to be 3D woven orthogonal.

Space vehicles that enter a planetary atmosphere like the Space Shuttle Orbiter (i.e. earth) require the use of a Thermal Protection System (TPS) to protect them from aerodynamic heating, which is generated at the surface of a space vehicle due to the combination of compression and surface friction of the atmospheric gas [60]. A TPS mainly is used to inhibit the heat entering into the vehicle [60, 61]. Due to the wide variation of temperatures, the TPS selected for a space shuttle is composed of many different materials. Each material's temperature capability, durability and weight determine the extent of its application on the vehicle [61]. The orbiter's nose cone, including the chin panel, and the leading edge of its wings are the hottest areas during re-entry [61]. During the reentry back

into the atmosphere, the maximum heating occurs about 20 minutes before touchdown , the maximum temperature on these surfaces can reach as high as 1700°C [61, 62]. Reinforced Carbon-Carbon composite (RCC), a light gray composite, along with Inconel foil insulators and quartz blankets, protect these areas from the highest expected temperatures and aerodynamic forces [62, 63].

The carbon fiber arrangement of RCC can be categorized into various constructions, including woven fabrics, three-dimensional (3-D) orthogonal, 2-D fabric laminated, isotropic [63]. Considering the oxidizing environments, the RCC must have oxidation protection coating. The common coating materials include SiC, Si_3N_4 and SiO_2 [63]. However, when temperature is as high as 1700°C, the thermal ablation/erosion speed is expected to be considerably high. If the coating layer erodes, the whole TPS will be damaged, therefore jeopardizing the safety

of a space vehicle. In this report, Perspirable Skin, a design to reduce the temperature of those hottest parts is proposed.

7.1 RCC Microstructures

Several types of RCC are compared in the following sections to find the optimized structure for carbon fiber arrangement, including 3-D orthogonal, 2-D fabric laminated and isotropic. Figure 7.1 shows the microstructure of a RCC composite sample (Agency for Defense Development (ADD), South Korea) at fiber-cutting direction and fiber-parallel direction.

In the preliminary design, the ZrW_2O_8 core is designed to be shrink-fit into the RCC skin. This shrink-fit process is expected to take place at high temperature where the size of the ZrW_2O_8 core has shrunk and the hole on the RCC skin has expanded. Therefore, they are expected to be assembled at high temperatures (above 800°C). At room temperature, the hole-diameter must be slightly smaller than the core diameter, causing the stresses on the core and the skin which guarantee a secure contact between the two parts at room temperature.

a

b

Figure 7.1: The representative microstructure of the RCC at a) fiber-cutting direction and b) fiber-parallel direction.

The design was performed by FEA Code ANSYS (Version 11.0). The gap between the ZrW_2O_8 and the RCC at the working temperature, 800°C, was determined. Additionally, the stresses on the contact surfaces between the two materials when the system is cooled down to room temperature were simulated. Several material properties has been inputted into the structural and thermal analyses, including Young's Modulus, Shear Modulus, Poisson's Ratio, CTE and thermal conductivity of each material.
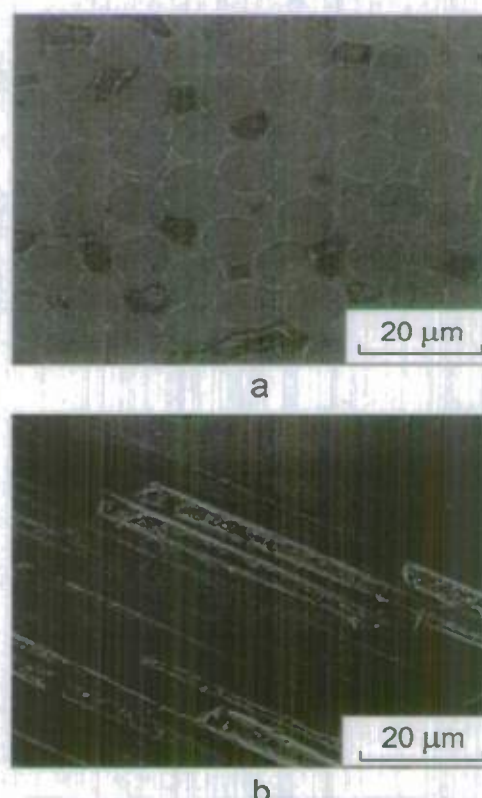
Most properties of the RCC used in FEA were taken from the report of Sheehan et al. [64], such as the Young's modulus, Shear modulus and CTE, which are listed in the Table 2. The CTE of isotropic RCC was tested from the RCC samples. The value also is shown in Table 2. The samples of RCC for CTE testing were rectangular parallelepipeds with edge lengths 10.6mm, 7.0mm and 7.0mm. The temperature dependence of thermal conductivity of RCC is based on the report of Savage [63], which is presented in Figure 7.2. The Poisson's ratio of RCC was taken as 0.2 based on the study of Tanabe et al. [65].
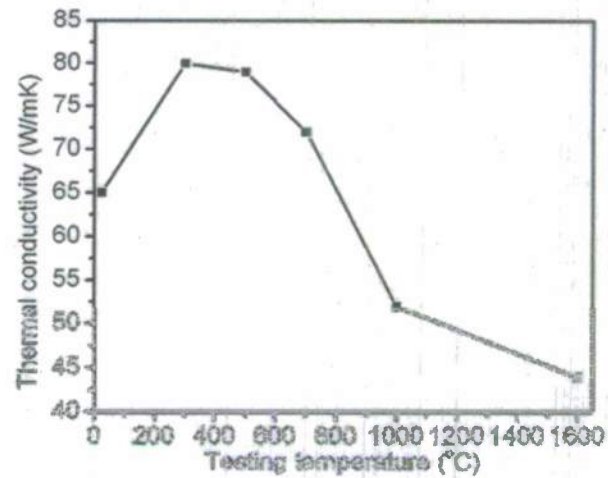

Figure 7.2: The temperature dependence of thermal conductivity of RCC [57].

TABLE 7.2 The VARIOUS PARAMETERS USED FOR RCC [58]

Designation	Young's Modulus (GPa)		Shear Modulus (GPa)	CTE ($10^{-6}K^{-1}$)	
	Longitudinal	Transverse		Longitudinal	Transverse
2D Fabric Laminate	118	4.1	6	1.3	6.1
3D Woven Orthogonal	55	96	17.5	1.3	1.3
3D Isotropic	14	-	-	2E-7**	2E-7**

**Testing results by the TMA.

7.2 FEA Modeling

The purpose of the FEA Modeling was to answer the best carbon fiber arrangement for the RCC, the determination of the dimensions that yield the largest gap distance and the geometry of the ZrW_2O_8 core for the coolant air. To answer the first question, we compared five RCC's, including 3D isotropic, 3D woven orthogonal, and three 2D laminates with $[0/45/-45/90]_s$ (quasi-isotropic), $[0/90]_s$ (cross-ply symmetric) and $[0/30/60/90/120/150]s$ fiber arrangements. Due to the distinct fiber structures in these five RCC, the mechanical and thermal properties are different as shown in Table 7.2. These variations finally result in different gap openings at the working temperature (i.e.: 800°C) and different stresses at the contact surface between RCC and ZrW_2O_8 at room temperature. For modeling layered composites such as laminated RCC, ANSYS offers a layered structural solid element (SOLID46). This element allows the user to input the thickness, orientation and material properties of each layer. In our design, the thickness of each layer was assumed to be 10μm, which is equal to the diameter of a carbon fiber. The total thickness of the structure was 8mm,

resulting in a total of 800 layers in the geometry. 3D isotropic and 3D woven orthogonal RCC, as well as the ZrW_2O_8 core were modeled using another structural element (SOLID45).

The ZrW_2O_8 core and the RCC skin were modeled as quarter-cylinder and quarter-hollow-cylinder respectively due to the symmetric structure. The axisymmetry was applied to both parts. Displacement boundary conditions were added to both parts. The corner edge (axisymmetry) of ZrW_2O_8 core was fixed in the x and y directions but was free to move in the z-direction. The boundary condition allows the core to expand and shrink in every direction. Additionally, the RCC skin will apply constraining force on the ZrW_2O_8 core so it will not move in the z-direction freely as discussed in the following section. The RCC skin was only constrained on the outer circular edge such that it could not move in the z-direction. This allows the skin to expand, shrink and bend as the actual skin in flight may experience.

To determine the gap distance between the two materials caused by the shrinkage of ZrW_2O_8 and the expansion of RCC in the assembling condition, the temperature was increased up to 800°C in the FEA model for both ZrW_2O_8 and RCC. At room temperature, the radius of the ZrW_2O_8 core was 15mm and the inner radius of the RCC was 14.98mm. The results showed that the ZrW_2O_8 core experienced the shrinkage of 0.082mm in radius. The expansion of the inner radius of the RCC varied depending on the fiber structure, thus the gap distance. Figure 7.3(a) shows the result for the isotropic RCC modeling. It was observed that [0/30/60/90/120/150]s RCC case give a non-uniform expansion and a gap distance, therefore this case was not further analyzed.

Next, both materials were cooled back down to room temperature and the stresses on the contact surfaces were compared. This two-step modeling process represents the whole assembly process. Figure 7.3(b) shows the stress result from the simulation with the isotropic RCC. The simulation results for the other four RCC models were similar. However, the gap distance and the stress values vary depending on the fiber arrangement. Table 7.3 shows the comparison of the simulation results as well as the tensile strengths for each RCC [64].
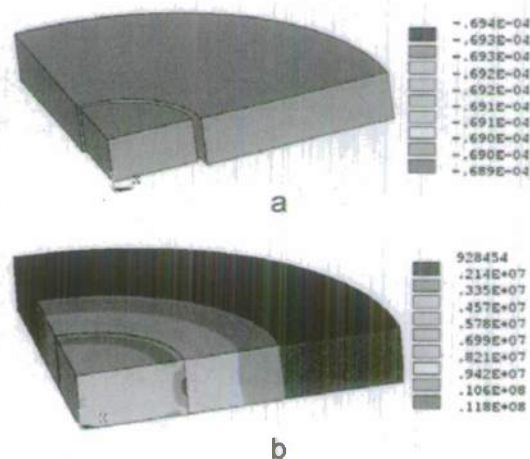

Figure 7.3: The simulation results for the isotropic RCC a) working/assembling temperature gap modeling and b) room temperature stress modeling.

TABLE 7.3: THE SUMMARY OF GAP DISTANCE AT 800°C WORKING TEMPERATURE AND THE STRESS AT ROOM TEMPERATURE (RT) BETWEEN ZRW₂O₈ CORE AND THE VARIOUS RCC SKIN

Designation	Gap (µm)	Stress (Mpa)	RT tensile strength (Mpa)*	
			Longitudinal	Transverse
3D Isotropic	64.41	11.7	41	5
3D Orthogonal	77.19	27.8	170	300
[0/45/-45/90]s	79.4	18.5	300-350	2.8-5.0
[0/90]s	79.4	18.8	300-350	2.8-5.0

*Data resource: [63, 64]

Obviously, the quasi-isotropic RCC ([0/45/-45/90]s) and cross-ply symmetric RCC ([0/90]s) resulted in the maximum gap distance of 79.4µm. However, for both structures, the maximum stress at room temperature exceeded the tensile strength in the transverse direction. This happens for the 3D isotropic RCC as well. Therefore, the best RCC structure for Perspirable Skin is the 3D woven orthogonal. Despite of the slightly lower gap distance resulting from the 3D woven orthogonal RCC, its highest tensile strength in both directions provide the best application for Perspirable Skin.

Optimizing the dimensions of the 3D woven orthogonal RCC to obtain a larger gap area for the coolant gas to exit is the second part of the FEA. By testing many inner radii of RCC skin, we found that a linear relationship exists between the gap distance and the inner radius of the RCC, as shown in Fig. 7.4. Maximum gap distance is achieved when the inner radius of RCC is 14.999mm; however, full contact between the two materials at room temperature is lost when inner radius of RCC is higher than 14.98mm. This means that RCC loses the contact on the ZrW₂O₈ core. In order to overcome this problem, new geometries, instead the simple cylinder, for the ZrW₂O₈ core/inner hole of RCC skin had to be considered.
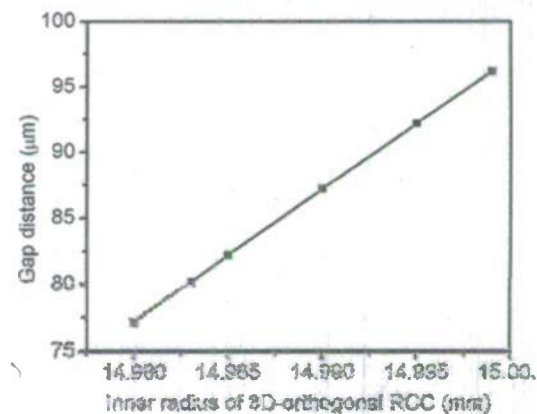

Figure 7.4: The relationship between the gap distance and the inner radius of 3D-orthogonal RCC

Under the working condition (during the reentry), a temperature gradient along the thickness is expected. The maximum temperature that the interior surface of RCC reaches is about 180°C as the outer surface is at 1700°C [61, 66]. With the cooling provided by Perspirable Skin, the outer temperature is expected to reach 800°C. The inner surface temperature may not be as high. Thus, the temperature gradient in the design was assumed to be 100°C for the interior layer and 800°C for the outer surface. As mentioned in the previous paragraph, the geometry of the ZrW_2O_8 core was changed to another shape which has a bigger radius at the top and a smaller radius at the bottom. When this new geometry experiences this temperature gradient, the top surface of the core will shrink significantly due to the endured high temperature resulting in a large gap at the top surface, while the bottom part of the core will still maintain contact with the RCC skin because of the much lower bottom temperature.

The first geometry considered consisted of two attached cylinders with the same height. At room temperature, the top cylinder had a radius of 15mm and the bottom one had a radius of 7.5mm. The inner radius of RCC was 14.995mm at the top and 7.49mm at the bottom. In order to model a thermal gradient throughout the material, a coupled thermal and structural analysis must be performed in ANSYS. For this reason two different material types must be used, one for the thermal analysis and one for the structural analysis. Figure 7.5(a) shows the gap opening for this new geometry under the temperature gradient mentioned above. The problem with the geometry shown in Figure 7.5(a) is that the bottom horizontal part of the upper cylinder stays in contact with the RCC, making it harder for the coolant gas to be channeled through the core and out to the exterior surface. Therefore, another shape of which the top part was tapered down resulting in a frustum of a cone with a top radius of 15mm and a bottom radius of 7.5mm was considered. The bottom part
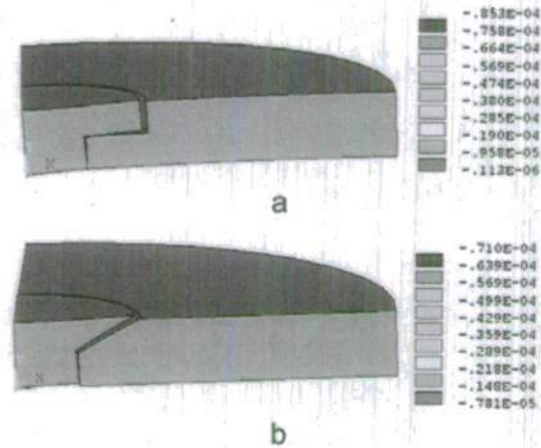

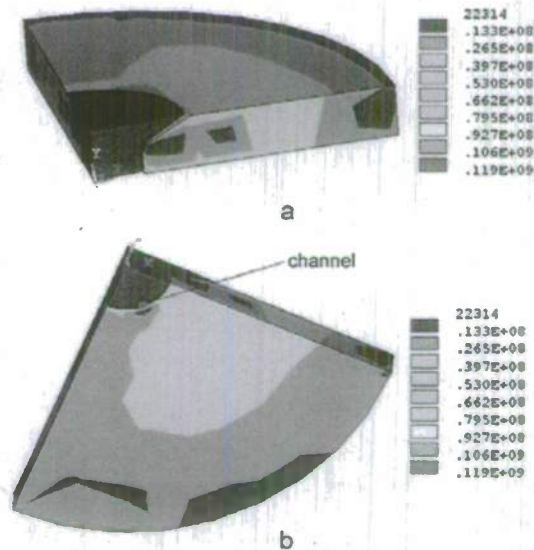Figure 7.5: The comparison of the gap shape and gap distance for the two shape designs.

Figure 7.6: The stress distribution at the operation condition for the tapered cone geometry design with 7.5 mm radius for the bottom cylinder and 1mm radius channels, a) side view and b) bottom view

remained cylindrical with a radius of 7.5mm. Figure 7.5(b) shows the gap distance of this structure under the 100-800°C temperature gradient. It can be clearly seen that this geometry provides a better and shorter route for the coolant gas. In order to achieve continuous flow path for the coolant gas, thin channels need to be incorporated into the cylindrical bottom half of the core. Semi-circular shaped channels starting from the bottom surface and extending half way up through the core has been simulated. These semi-circular channels had a 1mm radius and there were a total of 4 channels in the core geometry (one channel in the quarter-geometry). The incorporation of the thin channels does not change the gap distance. Figure 7.6 shows the stress contour of the bottom and side views at the working condition. The maximum stress of 119 MPa does not exceed the tensile strength of RCC in any directions. Therefore, this is the final design.

The design with tapered top does not provide a gap distance as large as the one with the cylindrical top. This is caused by the fact that the top portion has a larger dimension, yielding a smaller shrinkage. In order to compensate for this issue, the radius of the bottom cylinder of the ZrW_2O_8 core was increased. This increases the taper angle, resulting in a larger dimension of the core; thus, more shrinkage. Several larger radii were tested in order to investigate the relationship between gap distance and the radius of the bottom cylinder, as shown in Figure 7.6. It can be clearly seen that the gap distance increases with an increase in the bottom radius until 12mm is reached. For the radii larger than 12mm, the gap converges to $94.2\mu m$. Therefore, changing the bottom radius is an appropriate way to alter the gap distance.
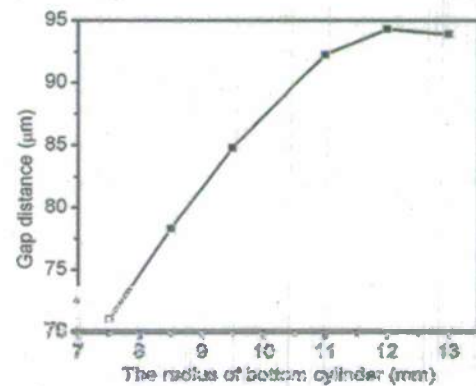

Figure 7.6: The relationship between the gap distance between the two materials and the bottom cylinder radius or the core

8. ZrW_2O_8-ZrO_2 CONTINUOUS FGM: FABRICATION AND THERMAL EXPANSION GRADIENT CONTROL

A ZrO_2+WO_3 powder mixture and ZrO_2 powder were stacked, co-compacted in a cylindrical die and co-sintered in the processing steps commonly used to fabricate multi-layer materials. However, the observation of the cross-sectional microstructures as well as the measurement of the radial thermal expansion indicate the evidence that the sintered samples are continuous Functionally Graded Materials (FGMs) made of ZrW_2O_8 and ZrO_2. Continuous FGM structures are formed by three mechanisms: 1) the diffusion of WO3, 2) the sublimation of WO_3 and 3) the reaction between ZrO_2 and WO_3. The variation in the soaking duration results in a variety of microstructures and CTE distribution for the sintered samples. Because of the discrepancy in the sintering potentials between two materials, the sintered FGM

samples do not retain the original cylindrical shapes of the green compacts. This problem has been resolved by choosing the appropriate powder mixture and controlling the shrinkage of each layer of the compacts. The continuous variation in the radial thermal expansion of the continuous FGM samples can be utilized to reduce the thermal stress induced from a thermal gradient loading within a material system. This study shows that the processing steps typically used in processing multi-layer FGMs can also be used to create continuous FGMs for some special powder mixtures.

8.1 Processing Method

Table 8.1 provides a summary of the four raw powders used in this study. The stoichiometric ratio of WO_3 and ZrO_2 was 2:1 (the mass ratio is mWO_3: $mZrO_2$ =1:0.266) in the WO_3+ZrO_2 powder mixture. This ratio is needed to produce pure $ZrW2O8$ by in-situ reaction of $WO3$ and ZrO_2 [1, 12]. All powder mixtures were mixed using 12mm-diameter zirconia media in a jar mill (U.S. Stoneware 764AVM, U.S.A.) for 48 hours. The WO_3+ZrO_2 powder mixture and $ZrO2$ powder were stacked layer-by-layer in a single-action die and then compacted under the compaction pressure of 80MPa to form two-layer ZrO_2/ZrO_2+WO_3 and three-layer $ZrO_2/ZrO_2+WO_3/ZrO_2$ green bodies. Each ZrO_2 layer was composed of 0.4g of zirconia powder. Four samples were produced, each featuring a unique mass ratio between the layers as shown in Table 8.2. Samples 1, 2 and 3 featured a symmetric $ZrO_2/ZrO_2+WO_3/ZrO_2$ stacking structure and the only variation among them was the mass of the mixture layer. Sample 4 was designed to have an asymmetric ZrO_2/ZrO_2+WO_3 stacking structure.

TABLE 8.1:. Four raw powders used in this study.

Name	Material	Mean particle size (µm)	Manufacturer
W-Fluka	WO_3	8.22	Sigma-Aldrich, U.S.A.
CERAC-2003[a]	ZrO_2	1.23	CERAC Inc., U.S.A.
TZ3YS[a]	ZrO_2	0.56	Tosoh Co., Japan
TMDAR	Al_2O_3	0.17	Taimei Chemical CO., LTD., Japan

[a]Stabilized by 3w% Y_2O_3.

TABLE 8.2. The mass ratio for each green sample and theoretical thickness/volume ratio and ZrW_2O_8 volume fraction in the sintered samples.

#	Mass ratio $m_{Zriconia1}$:$m_{Mixture}$:$m_{Zirconia2}$	Thickness/volume ratio $V_{Zriconia1}$:$V_{Mixture}$:$V_{Zirconia2}$	Theoretical ZrW_2O_8 volume fraction
1	1:1.78:1	1:2.13:1	51.5%
2	1:1.08:1	1:1.28:1	38.9%
3	1:0.65:1	1:0.77:1	29%
4	1:0.54:0	1:0.64:0	38.9%

The diameter of the green compacts was measured to be 7.94mm after compaction. Because the processing ZrW_2O_8 requires 1) the final soaking temperature higher than 1110°C and 2) a quenching step necessary to prevent the decomposition of ZrW_2O_8, these green compacts were sintered using the ramp/soak profile of Fig. 1 in a covered platinum crucible under atmospheric conditions in a furnace (Carbolite-HTF1700, UK). The covered crucible provided a nearly sealed environment in order to decrease the sublimation of WO_3 at temperatures higher than 800°C [67]. Three soaking durations of 3.5, 6 and 14 hours were employed to investigate its influence on the final microstructures. The volumes of the fully-sintered pieces were measured in water using Archimedes' principle for the calculation of the relative density.

Before the CTE testing, the samples were heat treated (3°C/min for both heating and cooling cycles, and soaking for 60 minutes at 300°C) to cure microcracks induced by the quenching process [47]. The CTE measurements of sintered samples were performed using a Thermomechanical Analyzer (TMA: Setaram 95, France) with argon gas providing a protective environment and using heating and cooling rates of 1°C/min. Three specimens produced for each sample were tested for their CTEs. The CTE variation in their measurement is less than 5%. Therefore, we considered that the CTE test results for each sample are consistent and each reported value is the average of the corresponding results of three specimens. The sintered samples were polished (Abramin, Denmark) and thermally etched in a furnace at 600°C. Then the microstructure of samples was observed using Scanning Electron Microscopy (JEOL 6400V, Japan).
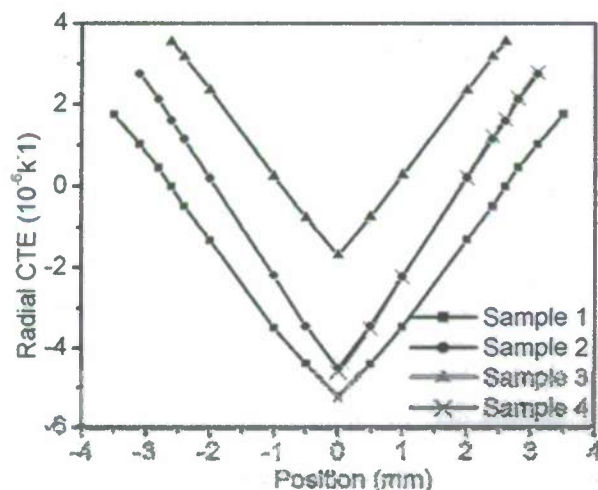
8.2 Continuous Material Gradient

Figure 8.1. The radial thermal expansion-position relationship for sintering FGMs at room temperature. The 0 position is the mid-plane for Sample 1-3 and the initial WO_3+ZrO_2 surface for Sample 4 (Soaking duration: 6 hours).

The radial surface of each sample was polished to achieve two parallel planes. The radial thermal expansions of each sample were then measured at several locations for each sample. It can be seen in Fig. 8.1 that the radial thermal expansions feature a continuously changing profile, providing additional evidence of a continuous gradient of the sintered FGMs. However, the radial expansions presented in Fig. 3 are not the physical properties of cross-sectional CTEs since the values include both the thermal expansion effect and the mechanical constraints exerted from the adjacent parts of the sample. After observing the microstructure of the cross-sections at each testing position, the corresponding ZrW_2O_8/ZrO_2 area ratio at each position was estimated. Using the graph

between CTE and ZrW_2O_8 volume fraction for ZrW_2O_8/ZrO_2 composites determined in the previous section, the corresponding cross-sectional CTE of each testing position was obtained. Figure 8.2 shows both the radial thermal expansion and the corresponding cross-sectional CTEs for Sample 4. Clearly, the discrepancy between two data is insignificant. However, since the adjacent parts have less ZrW_2O_8 proportion, the radial thermal expansion of the layers near the initial WO_3+ZrO_2 mixture surface show a slightly higher value then the cross-sectional CTEs due to the tension from the adjacent parts. The radial thermal expansion of the parts near the initial ZrO_2 surface are lower than the corresponding cross-sectional CTEs due to the compaction from the adjacent parts, which have more ZrW_2O_8 proportion. Due to the same reason, for Samples 1, 2 and 3, the central portions' radial CTEs are slightly higher than the cross-sectional CTEs and the outer surface parts' radial CTEs are a little lower.

There are several key processing factors that contribute to the fabrication of continuous FGMs. First, the soaking time was extended to 6 hours in order to fully react the constituent powders, WO_3 and ZrO_2. This ensures that the WO_3 powders have enough time to diffuse into the zirconia layer(s). Another major contributing factor that is essential to understanding this process is the sublimation of WO_3 at temperatures above 800°C [67]. The sublimation causes the WO_3 gas to diffuse into the whole crucible, providing an additional transport mechanism
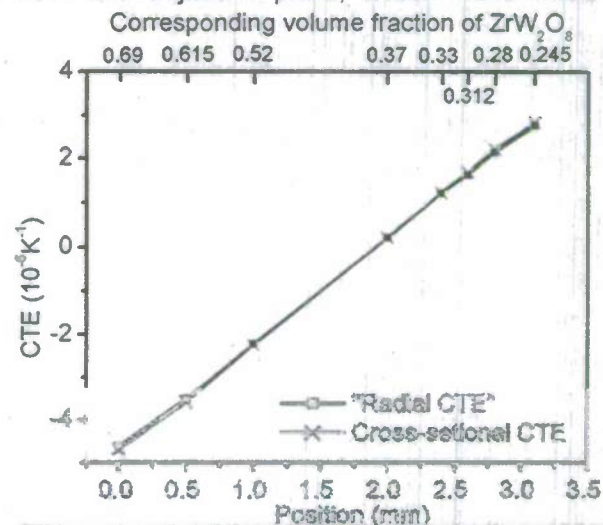

Figure 8.2: The radial thermal expansion and the corresponding cross-sectional CTEs for Sample 4 at room temperature. The sample height is 6.21mm. The 0 position is defined as the initial WO_3+ZrO_2 surface and the soaking duration was 6 hours

to form the continuously varying microstructures. The resulting transport of WO3 coupled with the chemical reaction between ZrO_2 and WO_3 enables the ZrW_2O_8 grains to appear not only in the initial WO_3+ZrO_2 mixture layer but also in the ZrO_2 layer(s). In addition, the symmetric distribution of WO_3 about the mid-plane in the green body for Samples 1, 2 and 3 contributed to the final symmetric distribution of ZrW_2O_8 throughout the sintered samples.

8.3 Influence of Soaking Duration on the Microstructures

Considering that the diffusion of WO_3 is one of the major contributing factors in the development of the continuous microstructure of the FGMs, the soaking duration must have a significant influence on the final microstructure. Therefore, two additional soaking durations, 3.5 and 14 hours, were evaluated. The samples sintered in these two new ramp/soak paths were also polished to observe the cross-sectional microstructures at several locations. For the samples sintered with the 3.5-hour soak time, the surfaces also show a gradual change in

yellow along the axial direction, similar to the sample processed with the 6 hours soak duration. The outermost surfaces of the initial ZrO_2 layers are now ZrW_2O_8/ZrO_2 composite structure in yellow color. However, most the other part of the initial ZrO_2 layers exhibited white circular regions surrounded by a yellow ring, in contrast to the whole yellow cross-section found in the previous samples. The microstructure observation showed that the outer ring is composed of both ZrO_2 and ZrW_2O_8 grains while the white center is composed of only zirconia. For Sample 2, the location of these "white circle + yellow ring" parts is between +2.4mm and +2.8mm and also between -2.4mm and -2.8mm along the axial direction using the origin of the coordinate defined at the center of the mid-plane. The whole height of the sample is 6.2mm and the sample occupies the space between -3.1mm and 3.1mm in the axial direction, and the initial WO_3+ZrO_2 powder mixture occupies the space between −1.21mm and 1.21mm. The white circle features a diameter of 6.91mm while the diameter of Sample 2 is 7.44mm, indicating that the central WO_3 did not diffuse into the whole ZrO_2 layer(s) with the 3.5-hour soaking duration. The average single-direction diffusion path of WO_3 in the ZrO_2 layer(s) for all four samples is only 1.2mm for the 3.5-hour soaking duration. Therefore, the average single-direction diffusion speed of WO_3 from the center part (initial mixture part) to the outer part (initial ZrO_2 part) is 0.343mm/hour. However, as pointed out above, the sublimation provides an additional transport mechanism for WO_3. This additional transport mechanism induces the formation of the yellow-colored $ZrW_2O_8+ZrO_2$ ring and the ZrW_2O_8/ZrO_2 composite structure for the outermost surfaces.

For the samples sintered with the 14-hour soaking time, the color distribution of the surfaces is even. The microstructure of each cut surface features a ZrW_2O_8/ZrO_2 composite structure and has nearly the same area fraction of ZrW2O8. This microstructural characteristic indicates the sintered samples are the even-distributed ZrW_2O_8/ZrO_2 composites. The volume fraction of ZrW_2O_8 for each sample is near to the theoretical value calculated by the mass ratio of ZrO_2 and WO_3 in Table 8.2. The measured radial thermal expansion also changed depending on the soaking duration. Figure 8.3 shows the radial thermal expansion for Sample 2. For the 3.5-hour soaking time, the "flat" sections represent no thermal expansion gradient. These "flat" portions occur at the locations similar to the "white circle + yellow ring." Therefore, the "flat" sections consist of the nearly pure ZrO_2 component. The decrease in the thermal expansion, the radial coordinates between +2.8mm and +3.2mm and also between -3.2mm and -2.8mm, which occurs due to the ZrW_2O_8 from the
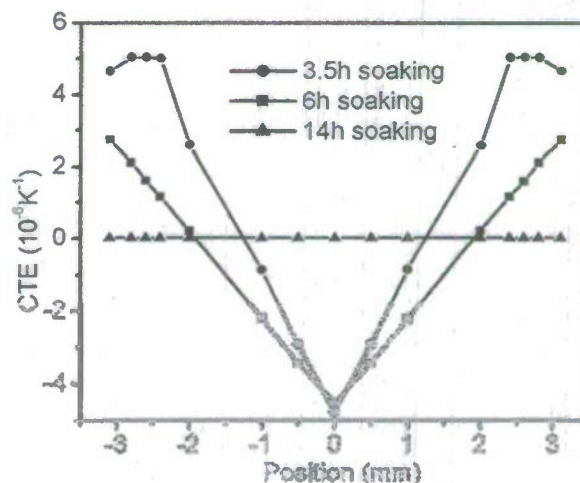

Figure 8.3. The CTE-position relationship of Sample 2 for various soaking durations.

reaction of ZrO_2 and sublimated WO_3. The radial thermal expansion of the samples with the 14-hour soaking time is nearly constant, which provides further evidence that the samples are evenly distributed ZrW_2O_8/ZrO_2 composites. Another important aspect to point out is that the radial thermal expansion values of the samples with the 14-hour soaking time are only slightly larger than the testing results for corresponding ZrW_2O_8/ZrO_2 composites with theoretical ZrW_2O_8 volume fraction calculated by the mass ratio of ZrO_2 and WO_3 (Table 8.2). This is due to the WO_3 that escaped the system as a gas produced by sublimation, resulting in a slight decrease of ZrW_2O_8 fraction in the samples.

8.4 Powder component change?

We changed the pure ZrO_2 powder in the stack to the powder with m_{WO3}: m_{ZrO2} =1:0.38 (Powder B) and keep the other powder m_{WO3}: m_{ZrO2} =1:0.266 (Powder A), here Powder A produces pure ZrW_2O_8 after sintering and Powder B produces a composite of ZrW_2O_8 and ZrO_2 with 0 CTE as mentioned in Section 6.1. 1.3g Powder A and 1.7g Powder B were measured and stacked together. After compaction and sintering by the same sintering process for pure ZrW_2O_8 (6 hours soak duration) a continuous $ZrW_2O_8+ZrO_2$ FGM was made. The height of the sintered sample is 7.7mm.

Figure 8.4. Measured CTE of the best FGM core design

The axial CTE of the sample is shown figure 11, which is near to the FEA requirement in Section 7.

8.5 Distortion Control

Initially, only CERAC-2003 powder was used for the zirconia components (both the WO_3+ZrO_2 powder mixture and ZrO_2 layer(s)). For the 3.5-hour and 6-hour soaking cases, after sintering, the original cylindrical shape of the green bodies changed to a shape similar to a barrel for Samples 1, 2 and 3 and the frustum of a cone for Sample 4. This distortion is a result of the final dimensional mismatch between the two materials. For the cylindrical green body with 7.94mm diameter sintered in the ramp/soak path from Fig. 1 with 6 hours soaking time, the ZrW_2O_8 produced by the in-situ reaction of WO_3 and ZrO_2 mixture (with the Stoichiometric ratio of 2:1) has a final diameter of 7.51mm while the pure CERAC-2003 yields only a 7.28mm diameter. Due to the variation in the proportion of ZrW_2O_8 along the axial direction, the diameter of the sample changes from the mid-plane (initial WO_3+ZrO_2 surface) to the outer surfaces (initial ZrO_2 surface).

Sun et al. [68] demonstrated that the compaction and sintering behaviors can be modified by mixing two or more powders with different initial powder characteristics of the same

material, ultimately influencing the final dimension of a sample. Based on this finding, CERAC-2003 powders were mixed with TZ3YS in a variety of proportions to form zirconia powder mixtures. The final diameters were changed as the proportion of CERAC-2003 in zirconia powder mixtures was varied, as shown in Figure 8.5. The relationship shown in Figure 8.5 can be explained by the fact that the two zirconia powders feature two distinct mean particle sizes (see Table 8.1). Thus, the powder mixing process will allow the smaller TZ3YS particles to fill in the interstitial spaces among the larger CERAC-2003 particles, producing a powder mixture with a better compaction capability than either TZ3YS or CERAC-2003. As a result, the final diameter of the sintered powder mixture sample is increased. Figure 8.5 shows
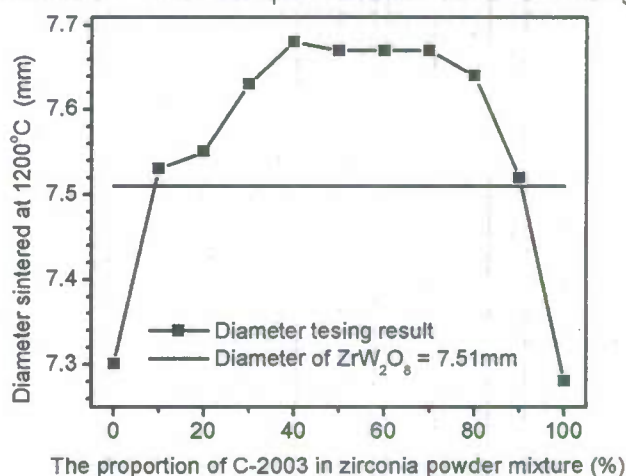

Figure. 8.5. The relationship between the diameters of zirconia samples sintered by the ramp/soak path with 6-hour soak duration and the percentage of Cerac-2003 in zirconia powder mixtures (the diameter of green bodies was 7.94mm).

that two mixtures of zirconia have a similar final diameter to the pure ZrW2O8 when the proportion of CERAC-2003 in zirconia system is around 8% or 91%. Through several attempts, the exact proportion of CERAC-2003 in the CERAC-2003+TZ3YS powder mixture has been refined to 11% in order to prevent the distortion in the sintered FGMs.

8.6 Density improvement

The final relative density of all four FGM samples was found to be only near 80%. As discussed, the samples exhibit this low density mainly because ZrO_2 is far from fully-sintered when the final soaking temperature is only 1190°C. This is evidenced in the micrograph where numerous pores remain among the ZrO_2 particles. In addition, the cracks between the ZrO_2 and ZrW_2O_8 grains due to the significant difference in CTEs between two component materials contribute to the low final density. In order to increase the final relative density, 0.07% mass ratio of the alumina powder TMDAR was added to each powder mixture, the same method also used. With the addition of alumina, a complex reaction occurs:

$$ZrO_2+WO_3+Al_2O_3 \rightarrow ZrW_2O_8+Al_2(WO_4)_3+ZrO_2+Al_2O_3 \qquad (1)$$

The melting point of $Al_2(WO_4)_3$ is 1135°C [69] and therefore a liquid phase exists at the soak temperature of 1190°C. The presence of this liquid will promote the densification kinetics, resulting in an increase in the final relative density. The addition of Al_2O_3 increased the final relative density from 80 to 90%. Furthermore, the final shape of the samples was not affected,

since the added TMDAR only comprises 0.07% of the total mass. The microstructure of the FGMs with 0.07% of Al_2O_3 remains very similar to that of Fig. 2. However, far fewer pores among ZrO_2 grains are evident, which can be attributed to the presence of the liquid $Al_2(WO_4)_3$ phase during sintering.

8.7 Axial CTEs

The axial CTE – temperature relation for all four samples (with 0.07% mass ratio TMDAR powder and 6 hours soaking duration) was measured and the data are presented in Fig. 7 together with the CTE curve of pure ZrW_2O_8. As can be seen, the macroscopic axial CTE is negative for Sample 1, positive for Sample 3 and nearly zero for Samples 2 and 4. The difference in the axial CTEs is due to the thickness variations in each layer for various samples. The CTE curves for all FGMs as well as the pure ZrW_2O_8 feature a sharp change near 160°C due to the α- to β-ZrW_2O_8 phase transition [70]. However, similar to the ZrW_2O_8/ZrO_2 composites, the peak caused by phase transition occurs at a lower temperature for the FGMs comparing to pure ZrW_2O_8. This "peak shift" is possibly a result of phase transition from α-ZrW_2O_8 (low pressure phase) to γ-ZrW_2O_8 (high pressure phase) [49] due to the thermal stresses caused by the CTE mismatch between ZrO_2 and ZrW_2O_8.

The axial CTEs of the samples processed under various soak durations are all close to the theoretical CTEs (Table 8.2) as shown in Table 8.3, which indicates that the average distribution ratio of ZrW_2O_8 along the axial direction does not changed for each soak duration. This observation attests to the diffusion mechanism mentioned earlier. We can conclude that even for 3.5-hour soak duration, all WO_3 have already reacted with ZrO_2 in the WO_3+ZrO_2 layer, thus generating a sharp boundary between $ZrW_2O_8+ZrO_2$ and pure ZrO_2. For Sample 2, the boundaries were at the 2.4mm position mentioned before. As the soak duration increases, due to the different concentration of ZrO_2 across the boundary, the ZrW_2O_8 in the $ZrW_2O_8+ZrO_2$ layer partially decomposes and produces WO3.   The new WO_3 diffuses toward the pure ZrO_2 layer and react with the ZrO_2 to produce new ZrW_2O_8. Thus, the ZrW_2O_8 decomposes and the products react during the processing.   With this decomposition-reaction mechanism, ZrW2O8 advances toward the outer surfaces of ZrO_2 layer(s). Therefore, the important processing technique in the fabrication of fully continuous FGMs requires appropriately adjusting soaking duration. However, the gradient of ZrO_2 in the FGMs will drive the decomposition-reaction mechanisms to continue if the soak duration continually increases until the sample becomes the evenly distributed ZrW_2O_8/ZrO_2 composite, as evident by the 14-hour soak duration case. However, due to the loss of WO_3 by sublimation, the CTE values of the samples after the 14-hour sinter duration are slightly larger than the theoretical values.

The continuous radial thermal expansion variation of the FGMs can be utilized to reduce the thermal stress induced from a thermal gradient loading that may exist in a structure. Considering the processing method described here, several other ceramic mixture systems such as $ZnO+Nb_2O_5$ and $Sb_2O_3+Al_2O_3$ may also have the potential to produce continuous

FGMs.

9. CONCLUSION

The Perspirable skin has been designed and the important components of the Perspirable Skin such as the core have been designed in more detail and fabricated. To enable shrink-fit process of the core into the skin, powder compaction and sintering behaviors of ceramic powders have been extensively studied. For the application of supersonic and reentry vehicles, the skin made RCC with orthogonal woven structure and the Functionally Graded Materials core made of Zicornia Tungstate and Zirconia are chosen. The designed perspirable skin, however, utilizes the in-plane deformation due to the thermal gradient loading. In the next generation of Perspirable Skin, out-of plane deformation will be utilized to yield much larger interference, which provide a much more efficient self-cooling capability.

REFERENCES

1.   Roy, R., Agrawal D.K., MacKinstry H.A., Very low thermal expansion coefficient materials, Annu. Rev. Mater. Sci., 1989, 19, 59-81

2.   Mittal, R. and Chaplot S.L., Lattice dynamical calculation of isotropic Negative Thermal Expansion in ZrW2O8 over 0-1050K., Phys. Rev. B, 1999, 60, Bo.10, 7234-7237

3.   Savage G., Carbon-Carbon Composites., Chapman & Hall, 1993, 1st edition

4.   Evans J.S.O., Mary T.A. and Sleight A.W., Negative thermal expansion material, Phys. B., 1998, 241-243, 311-316

5.   Mary, T.A., Evans, J.S.O., Vogt, T. and Sleight, A.W., Negative thermal expansion from0.3 to 1050 Kelvin in ZrW_2O_8., Science, 1996, 272, 90-92

6.   Yilmaz, S., Phase transformations in thermally cycled Cu/ZrW_2O_8 composites investigated by synchrotron x-ray diffraction, J. Phys. Cond. Mater. 2002, 14, 365-375

7.   Westman A. E. R., and Hugill H. R. The packing of particles, J. Am. Ceram. Soc. 13 (1932), pp. 767–779.

8.   McGeary R. K., Mechanical packing of spherical particles, J AM Ceram Soc 44(10) 1961 513-522

9.   Aydin, I., Briscoe, B., and Sanliturk, K. Y., Density distributions during the compaction of alumina powders: a comparison of a computational prediction with experiment, Computational Materials Science 1994 3 55-68.

10. Aydin, I., Briscoe, B., and Sanliturk, K. Y., Dimensional variation of die-pressed ceramic green compacts: comparison of a finite element modeling with experiment, Journal of European Ceramic Society, 1997 17 1201-1212.

11. Sun, L., Sneller, A. and Kwon, P., Fabrication of Alumina/Zirconia Functionally Graded Material: From Optimization of Processing Parameters to Phenomenological Constitutive Models, Mater. Sci. Eng. A, 2008, 488, 1-2, 31-38

12.   Liu D. M. and Lin J. T, Influence of ceramic powders of different characteristics on

particle packing structure and sintering behavior, Journal of Materials Science, 1999, 34, 1959-1972

13.   He D., Ekere M. N. and Cai L., Computer simulation of random packing of unequal particles, Physical Review E, 1999, 60, 7098   .

14.   Brouwers H. J. H., Particle-size distribution and packing fraction of geometric random packings, Physical Review E, 2006, 74, 031309- 1-14.

15.   Aydin, I. Briscoe B. J. and Sanliturk K. Y. The internal form of compacted ceramic components: a comparison of a finite element modeling with experiment, Powder Technol. 1996, 89, 239-254

16.   Train D, Transmission of forces through a powder mass during the process of pelleting. Trans. Instn. Chem. Engrs, 1957, 35, 258-266

17.   Schwartz, E. G. and Weinstein A. S., Model for compaction of ceramic powders. J Amer. Ceram. Soc., 1965, 48, 346-350

18.   Macleod, H. M. and Marshall, K., The determination of density distributions in ceramic compacts using autoradiography. Powder Technol., 1977, 16, 107-122

19.   Kwon, Y. S. and Kim K. T. Densification forming of alumina powder-effects of powder law creep and friction, J Eng. Mat. Techno. 1996, 118, 471-455.

20.   Reed J. S., Introduction of the Principles of Ceramic Processing, 1988, John Wiley & Sons, 185-199.

21.   Kwon, Y. S. and Kim, K. T., High-temperature densification forming of alumina powder-constitutive model and experiments, ASME J. Eng. Mat. Tech., 1996, 118, 448-455.

22.   Gillia, O. and Bouvard, D., Phenomenological analysis of densification kinetics during sintering: application to WC-Co mixture, Mat. Sci. Eng. A, 2000, A279, 185-191.

23.   Kim, H., Olivier, G. and Bouvard, D., A phenomenological constitutive model for the sintering of alumina powder., J. Eur. Ceram. Soc., 2003, 23, 1675-1685.

24.   Gillia, O., Josserond, C. and Bouvard, D., Viscosity of WC-Co compacts during sintering., Acta Mater., 2001, 49, 1413-1420.

25.   Handwerker, C.A., Morris P.A. and Coble R.L., Effects of chemical inhomogeneities on grain growth and microstructure in alumina, J. Am. Ceram. Soc., 1989, 72, 130-136

26.   Bae, I.J. and Baik S., Abnormal grain growth of alumina, J. Am. Ceram. Soc., 1997, 80, 1149-1156

27.   Woolfrey J. and Bannister M. J., Nonisothermal techniques for studying initial-stage sintering, J. Am. Ceram. Soc., 1972, 55, 390-394

28.   D.Lance, F. Valdivieso and P.Goeuriot, Correlation between densification rate and microstructural evolution for pure alpha alumina, J. Eur. Ceram. Soc., 2004, 24, 2749-2761

29.   Ting J.M. and Lin R. Y., Effect of particle size distribution on sintering: Part I Modeling., J. Mater. Sci., 1994, 29, 1867-1872

30.   Ting J.M. and Lin R. Y., Effect of particle size distribution on sintering: Part I Sintering of alumina., J. Mater. Sci., 1995, 30, 2382-2389

31.   Kim, H. G., Lee, H. M. and Kim, K. T., Near-net-shape forming of ceramic powder under cold combination pressing and pressureless sintering, ASME J. Eng. Mat. Tech., 2001, 123,

221-228.

32.   Du, Z. Z., Cocks, A. C. F., Constitutive models for the sintering of ceramic components. II. Sintering of inhomogeneous bodies, Acta Metall. Mater., 1992, 40, 1981-1994.

33.   Rahaman M. N, De Jonghe L.C. and Chu M. Y., Effect of green density on densification and creep during sintering, J. Am. Ceram. Soc., 1991, 74, 514-519

34.   Chu, M. Y., Rahaman, M.N. and De Jonghe L.C., Effect of heating rate on sintering and coarsening. J. Am. Ceram. Soc., 1991, 74, 1217-1225

35.   McHugh, P. E. and Riedel, H., A liquid phase sintering model: application to Si_3N_4 and WC-Co., Acta Mater., 1997, 45, 2995-3003.

36.   Svoboda, J., Riedel, H. and Zipse, H., Equilibrium pore surfaces, sintering stresses and constitutive equations for the intermediate and late stages of sintering. I. Computation of equilibrium surfaces, Acta   Metall. Mater., 1994, 42, 435-443.

37.   Dorn, J.E. Creep, Recovery, American society for metals, Cleveland, Oh, 1957, 255-283.

38.   Hsueh, C. H., Evans, A. G., Cannon, R. M. and Brook, R. J., Viscoelastic stresses and sintering damage in heterogeneous powder compacts., Acta Metall., 1986, 34, 927-936.

39.   K.T. Kim, S.W. Choi, H. Park, Densification Behavior of Ceramic Powder under Cold Compaction, Journal of Engineering Materials and Technology 122 (2000) 238–244.

40.   D.H. Zeuch, J.M. Grazier, J.G. Argüello, K.G. Ewsuk, Mechanical properties and shear failure surfaces for two alumina powders in triaxial compression J. Mats. Sci. 36 (2001) 2911–2924.

41.   F.R. Charvat, W.D. Kingery, J. Am. Ceram. Soc. 40 (1957) 306–315.

42.   M.R. Winter, D.R. Clarke, J. Am. Ceram. Soc. 90 (2007) 533–540.

43.   P.Z. Cai, D.J. Green, G. L. Messing, J. Am. Ceram. Soc. 80 (1997) 1929–1939.

44.   R. Torrecillas, A.M. Espino, J.F. Bartolomé, J.S. Moya, J. Am. Ceram. Soc. 83 (2000) 454–456.

45.   C.Legros, C.Carry, P.Bowen, H.Hofmann, J. Eur. Ceram. Soc. 19 (1999) 1967-1978

46.   Kuribayashi K, Yoshimura M, Ohta T, Sata T. High-temperature phase relations in the system Y2O3-Y2O3•WO3. J Am Ceram Soc 1980;63(11-12):644-647.

47.   Chen J. C, Huang G. C, Hu C, Weng J. P. Synthesis of negative-thermal-expansion ZrW2O8 substrates. Scripta Mater 2003;49(3):261-266.

48.   Chang L. Y, Scroger M. G, Phillips B. Condensed phase relations in the systems ZrO2-WO2-WO3 and HfO2-WO2-WO3. J Am Ceram Soc 1967; 50(4):211-215.

49.   Jorgensen J. D, Hu Z, Teslic S, Argyriou D. N, Short S, Evans J. S. O, Sleight A. W. Pressure-induced cubic-to-orthorhombic phase transition in ZrW2O8. Phys Rew B 1999; 59(1):215-225.

50.   Turner P. S. Thermal Expansion Stresses in Reinforced Plastics. J Res Natl Bureau Stand 1946; 37:239-245.

51.   Kerner E. H. The Elastic and Thermo-Elastic Properties of Composite Media. Proc Phys Soc B 1965;69:808-813.

52.   Rosen B.W, Hashin Z. Effective thermal expansion coefficients and specific heats of composite materials. Int J Eng Sci 1970;8(2):157-173

53. Levin V. M. Thermal expansion coefficients of heterogeneous materials, Mekhanika Tuerdogo Tela, 1967;2(1):88-94.

54. Hsieh C. L, Tuan W. H. Thermal expansion behavior of model ceramic-metal composite. Mater Sci Eng A 2007;460-461(1):453-458

55. DryMiotis F. R, Ledbetter H, Betts J. B, Kimura T, Lashley J. C, Migliori A, Ramirez A. P, Kowach G. R, Van Duijn J. Monocrystal elastic constants of the negative-thermal-expansion compound Zirconium Tungstate (ZrW2O8). Phys Rev Lett 2004; 93(2):025502.

56. Adams J. W, Ruh R. Mazdiyasni K. S. Young's modulus, flexural strength and fracure of yttria-stailized zirconia versus temperature. J Am Ceram Soc 1997;80(4):903-908.

57. Holcome C. E, Meek T. T, Dykes N. L. Unusual properties of microwave-sintered yttria-2wt% zirconia. J Mater Sci Lett 1988;7(8):881-884.

58. Kwon P and Dharan C.K. H. Effective moduli of high volume fraction particulate composites. Acta Metall Mater 1995; 43(3):1141-1147.

59. Achary S. N, Mukherjee G. D, Tyagi A. K, Vaidya S. N. Preparation, Thermal expansion, high Pressure and high temperature behavior of $Al_2(WO_4)_3$. J Mater Sci 2002;37(12): 2501-2509.

60. Angelo, J. A., 1999, "The dictionary of space technology," New York: Facts on File, pp.211-225.

61. Cleland, G. G., 1989, "Thermal protection system of the space shuttle," NASA contractor report: NASA CR-4227.

62. Richard, S., 1980, "Orbiter Protective Tiles Assume Structural Role," Aviat Week & Spa Tech., Feb.25, pp22-24.

63. Savage, G., 1993, "Carbon fibres" & "Application of carbon-carbon composites," New York: Chapman & Hall, Carbon-carbon composites, pp37-80 & pp. 322-332.

64. Sheehan, J. E., Buesking, K. W., Sullivan, B. J., 1994, "Carbon-Carbon Composites," Annu. Rev. Mater. Sci.,24, pp. 19-44.

65. Tanabe, Y., Yasuda, E., Kimura, S., Iseki, T., Maruyama, T., Yano, T., 1991, "Neutron irradiation effects on dimension and mechanical properties of carbon fiber/carbon composite," Carbon 29 (7), pp. 905-908.

66. Barber, D., 2000, "Thermal barriers Oceaneering thermal systems," NASA Seal/Secondary Airflow System Workshop, OTS Thermal Barriers.

67. Kuribayashi K, Yoshimura M, Ohta T, Sata T. High-temperature phase relations in the system Y_2O_3-Y_2O_3•WO_3. J Am Ceram Soc 1980; 63(11-12):644-647.

68. Sun L, Sneller A, Kwon P. Fabrication of Alumina/Zirconia Functionally Graded Material: From Optimization of Processing Parameters to Phenomenological Constitutive Models. Mater Sci Eng A. 2007;doi:10.1016/j.msea.2007.10.044.

69. Achary S. N, Mukherjee G. D, Tyagi A. K, Vaidya S. N. Preparation, Thermal expansion, high Pressure and high temperature behavior of Al2(WO4)3. J Mater Sci . 2002; 37(12): 2501-2509.

70. Mary T. A, Evans J. S. O, Vogt T, Sleight A. W. Negative thermal expansion from 0.3 to 1050 Kelvin in ZrW2O8. Science 1996; 272(5258): 90-92.

Personnel Supported

Patrick Kwon
Hongjoo Rhee (Post-doc)
Ben Souder (Summer Undergraduate Research Experience)
Dennis Sumanski (Summer Undergraduate Research Experience)
Sun Li (Ph. D. Student)
Bhushan Ekbote (M.S.)
Kyung Hee Park (M.S. Student)
Basak Oguz (M.S. Student)
Adam Sneller and Agatha Bones (Undergraduate Students)

Publications

B. Ekbote, P. Kwon and M. Prime, 2006, "Micromechanics-based Design and Processing of Efficient Meso-scale Heat Exchanger," American Composite Society.

B. K. Paul, P. Kwon and R. Subramanian, 2006, "Limits on Aspect Ratio in Two-Fluid Micro-Scale Heat Exchangers," ASME Transactions, Journal of Manufacturing Science and Engineering, 128, pp. 977-983.

Li, S., Sneller, A.., Bone, A.and P. Kwon, 2007, "The influence of powder size distribution on sintering behavior," 22nd Annual Technical Conference of the American Society for Composites, Seattle, WA.

Li, S., Park, K. Y. and P. Kwon, 2007, "Minimizing Camber by controlling the influence factors in powder processing of zirconia/alumina functionally graded material," 22nd Annual Technical Conference of the American Society for Composites, Seattle, WA.

Li, S. and Kwon*, P., 2008," Powder Selection for Cosintering Multi-layered Ceramic FGM Based on the Densification Kinetics Curves," *Journal of Composite Materials*, accepted.

Li, S., Snellor, A. and P. Kwon*, 2008, 'ZrO2+ZrW2O8 Composites with Near-Zero Coefficient of Thermal Expansion Fabricated by Various Methods: Comparison and Optimization," *Composite Science and Technology*, 68, pp. 3425-3430.

Li Sun, P. Kwon*, D. Kim and K. Beaver, 2008, "Progress Toward A Denser Metal Matrix Composite Using the Three Dimensional Printing Method," Transaction of NAMRII/SME, XXXVI, pp. 105-112.

Li, S., Sneller, A., Kwon*, P., 2008, "Fabrication of Alumina/Zirconia Functionally Graded Material: From Optimization of Processing Parameters to Phenomenological Constitutive Models," *Materials Science and Engineering A*, 448, 1-2, pp. 31-38.

Li, S. and Kwon*, P., 2008, "In-Situ Reaction of ZrO_2+WO_3, Part I: ZrW_2O_8/ZrO_2 Composites: Processing, Properties and Theoretical Model Predictions," ACTA Metal., submitted,

Li, S. Kwon*, P., 2008, "In-Situ Reaction of ZrO_2+WO_3, Part II: $ZrW_2O_8-ZrO_2$ Continuous Functionally Graded Materials: Processing and the Influence of Soaking Duration on Microstructures," ACTA Metal., submitted.

B. Oguz, L. Sun and P. Kwon, "Perspirable Skin: A Multifunctional Material System For Self-Cooling," ASME Conference on Smart Materials, Adaptive Structures and Intelligent Systems, SMASIS2008, October 28-30, 2008, Ellicott City, Maryland, USA

S. Li, A. Sneller, S. Baldauf and P. Kwon, 2008, "Processing of $Zrw_2O_8-ZrO_2$ Continuous Functionally Graded Materials by Co-Sintering ZrO_2 and ZrO_2+WO_3 Multi-Layer Compacts," International Manufacturing Science and Engineering Conference, Evanston, IL .

Interactions/Transactions

P. Kwon, 2005, presentation at JSME/ASME International Conference on Materials and Processing.
P. Kwon, 2006, presentation at American Composites Society Conference on Materials and Processing.
P. Kwon, 2006, presentation at AFOSR Contractors' Meeting, Seattle, WA.
P. Kwon, 2007, presentation at American Composites Society Conference on Materials and Processing.
P. Kwon, 2007, presentation at AFOSR Contractors' Meeting, Monterey, CA.
P. Kwon, 2008, presentation at AFOSR Contractors' Meeting, Arlington, VA.
S. Li, 2008, presentation at American Composites Society Conference on Materials and Processing.
P. Kwon, 2008, presentation at International Conference of Manufacturing Science and Engineering and JSME/ASME International Conference on Materials and Processing.

New Discoveries, Inventions or Patent Disclosure

Invention Disclosure Number 07-074F on November 2, 2006.